

## 1 **Extrinsic and Intrinsic Dynamics in Movement Intermittency**

2 Damar Susilaradeya<sup>1</sup>, Wei Xu<sup>1</sup>, Thomas M Hall<sup>1</sup>, Ferran Galán<sup>1,2</sup>, Kai Alter<sup>1</sup>, Andrew Jackson<sup>1</sup>

3 1. *Institute of Neuroscience, Faculty of Medical Sciences, Newcastle University, Newcastle NE2 4HH,*  
4 *UK*

5 2. *Current address: Department of Basic Neuroscience, Faculty of Medicine, University of Geneva, CH-*  
6 *1202 Genève*

### 7 **Abstract**

8 What determines how we move in the world? Motor neuroscience often focusses either on intrinsic  
9 rhythmical properties of motor circuits or extrinsic sensorimotor feedback loops. Here we show that  
10 the interplay of both intrinsic and extrinsic dynamics is required to explain the intermittency observed  
11 in continuous tracking movements. Using spatiotemporal perturbations in humans, we demonstrate  
12 that apparently discrete submovements made 2-3 times per second reflect constructive interference  
13 between motor errors and continuous feedback corrections that are filtered by intrinsic circuitry in  
14 the motor system. Local field potentials in monkey motor cortex revealed characteristic signatures of  
15 a Kalman filter giving rise to both low-frequency cortical cycles during movement, and delta  
16 oscillations during sleep. We interpret these results within the framework of optimal feedback control,  
17 and suggest that the intrinsic rhythmicity of motor cortical networks reflects an internal model of  
18 external dynamics which is used for state estimation during feedback-guided movement.

### 19 **Keywords**

20 Submovements, movement intermittency, motor cortex, optimal feedback control

### 21 **Introduction**

22 Many visually-guided movements are characterized by intermittent speed fluctuations. For example  
23 while tracking slowly-moving targets, humans make around 2-3 submovements per second. Although  
24 first described over a century ago (Woodworth, 1899; Craik, 1947; Vince, 1948) the cause of  
25 movement intermittency remains debated. Submovements often disappear in the absence of vision  
26 (Miall *et al.*, 1993a) and are influenced by feedback delays (Miall, 1996), suggesting their timing  
27 depends on extrinsic properties of visuomotor feedback loops. However, rhythmicity is also reported  
28 in the absence of feedback (Doeringer and Hogan, 1998), and it has been suggested that an internal  
29 refractory period, clock or oscillator parses complex movements into discrete isochronal segments  
30 (Viviani and Flash, 1995; Russell and Sternad, 2001; Loram *et al.*, 2006; Hogan and Sternad, 2012).  
31 Cyclical dynamics within motor cortical networks with a time period of 300-500ms may reflect the  
32 neural correlates of such an intrinsic oscillator (Churchland *et al.*, 2012; Hall *et al.*, 2014). During  
33 continuous tracking, each submovement is phase-locked to a single cortical cycle, giving rise to low-  
34 frequency coherence between cortical oscillations and movement speed (Jerbi *et al.*, 2007; Hall *et al.*,  
35 2014; Pereira *et al.*, 2017). Moreover, this rhythmicity appears conserved across a wide range of  
36 behaviors and even shares a common dynamical structure with delta oscillations during sleep (Hall *et al.*  
37 *et al.*, 2014). It has been proposed that recurrent networks express these intrinsic dynamics as an ‘engine  
38 of movement’ responsible for internal generation and timing of the descending motor command  
39 (Churchland *et al.*, 2012). Nevertheless, the interplay between intrinsic rhythmicity and extrinsic  
40 feedback remains poorly understood. For example, if feedback delays influence submovement timing  
41 they might be expected also to alter the frequency of cortical cycles. However, this seems  
42 incompatible with conserved intrinsic dynamics evident across multiple behavioral contexts including  
43 sleep. Moreover, the precise computational role of such intrinsic circuitry remains uncertain.

44 In recent years, stochastic optimal control theory has emerged as an influential computational  
45 approach to understanding human movement, due to recognition of the impact of noise in both motor  
46 and sensory signals on behavior (Todorov and Jordan, 2002; Scott, 2004). In the presence of delayed,  
47 uncertain measurements, feedback should act on optimal estimates of the discrepancy between  
48 desired goals and current motor states. Optimal feedback control (OFC) explains many features of  
49 movement but it is unclear whether optimality principles alone can account for movement  
50 intermittency. Various modifications to OFC have been proposed, for example explicitly including a  
51 refractory period between submovements (Gawthrop *et al.*, 2011), but theoretical justification for  
52 these additions is lacking. Here we present evidence from visuomotor tracking by humans and non-  
53 human primates in support of an OFC-based model of movement intermittency that does not require  
54 explicit parsing of submovements. Instead, continuous integration of external feedback with internal  
55 state estimation provides a framework for understanding both extrinsic and intrinsic contributions to  
56 intermittency. This can account for many puzzling features of submovements, and provides a  
57 parsimonious explanation for conserved cyclical dynamics in motor cortex networks during behavior  
58 and sleep.

59

## 60 Results

### 61 *Submovements reflect constructive interference between motor noise and delayed feedback* 62 *corrections*

63 Human subjects generated bimanual isometric index finger forces to track targets that moved in 2D  
64 circular trajectories with constant speed (Fig. 1A). We measured intermittency in the angular velocity  
65 of the cursor (Fig. 1B, C), using spectral analysis to quantify submovement frequencies. Under normal  
66 feedback conditions, power spectra generally exhibited a principal peak at around 2 Hz (Fig. 1D) and  
67 this frequency was only slightly affected by target speed (Figure S1), consistent with previous  
68 descriptions of movement intermittency (Miall, 1996). However, submovement frequencies were  
69 markedly altered when visual feedback of the cursor was delayed relative to finger forces. With delays  
70 of 100 and 200 ms, the frequency of the primary peak reduced to around 1.4 and 1 Hz respectively  
71 (Fig. 1D, Fig. S1, Fig. S2), suggesting submovement timing was not determined by a fixed internal clock  
72 but depended instead on extrinsic feedback properties. Interestingly, a further peak appeared at  
73 approximately three times the frequency of the primary peak and, with increased delays of 300 and  
74 400 ms, a 5<sup>th</sup> harmonic was observed. The time-periods of the first, third and fifth harmonics were  
75 linearly related to extrinsic delay times with gradients of  $1.89 \pm 0.20$ ,  $0.59 \pm 0.04$  and  $0.33 \pm 0.11$   
76 respectively (Fig. 1E, Table S1).

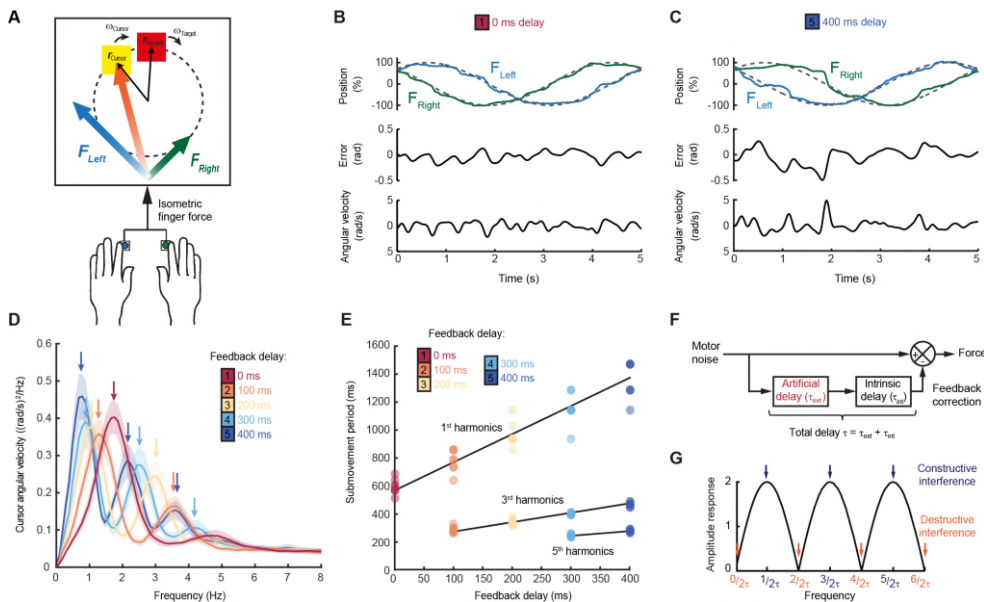
77 These results are consistent with a feedback controller responding to broad-spectrum (stochastic)  
78 tracking errors introduced by noise in the motor output, for which the response is delayed by time  $\tau$   
79 (Fig. 1F). In signal processing terms, subtracting a delayed version from the original signal is known as  
80 comb filtering. For motor noise components with a time period,  $T = \tau/1, \tau/2, \tau/3 \dots$ , delayed  
81 feedback accurately reflects current errors, resulting in regularly spaced notches in the amplitude  
82 response of the system (Fig. 1G) and attenuation from the resultant cursor movement through  
83 destructive interference. By contrast, for motor noise with a time-period,  $T = 2\tau/1, 2\tau/3, 2\tau/5 \dots$ ,  
84 delayed feedback is exactly out-of-phase with the current error. Thus, corrective movements  
85 exacerbate these components through constructive interference leading to spectral peaks at  
86 frequencies:

$$87 \quad f = 1/T = N/2(\tau_{\text{int}} + \tau_{\text{ext}}) \text{ with } N = 1, 3, 5 \dots \quad (\text{Equ. 1})$$

88 Submovement frequencies in our data approximately matched this model assuming the total feedback  
 89 delay comprised the experimental manipulation  $\tau_{ext}$  added to a constant physiological response  
 90 latency  $\tau_{int}$  of around 300 ms (Table S1), comparable to visual reaction times.

91 Note that in this interpretation, intermittency arises not from active generation of discrete  
 92 submovement events but as a byproduct of continuous, linear feedback control with inherent time  
 93 delays. Submovement frequencies need not be present in the smooth target movement, nor do they  
 94 arise from controller non-linearities. Instead these frequencies reflect components of broad-band  
 95 motor noise that are exacerbated by delayed feedback corrections. To seek further evidence that  
 96 intermittency arises from constructive interference between motor noise and delayed feedback  
 97 corrections, we generated artificial errors during target tracking by adding spatial perturbations to the  
 98 cursor displayed to subjects. Within individual trials, a sinusoidal displacement was applied in a  
 99 direction aligned to target motion and at a frequency between 1-5 Hz. Perturbation amplitudes were  
 100 scaled to have equivalent peak angular velocities (equal to the angular velocity of the target). Our  
 101 hypothesis was that artificial errors at submovement frequencies would be harder to track (because  
 102 of constructive interference) than perturbations at frequencies absent from the velocity spectrum.

103



104

105 **Figure 1. Movement intermittency during visuomotor tracking depends on feedback delays.** (A)  
 106 Schematic of human tracking task. Bimanual isometric finger forces control 2D cursor position to track  
 107 slow, circular target motion. Kinematic analyses use the angular velocity of the cursor subtended at  
 108 the screen center screen. (B) Example force (*top*), angular error (*middle*) and cursor angular velocity  
 109 (*bottom*) traces during target tracking with no feedback delay. Submovements are evident as  
 110 intermittent fluctuations in angular velocity. (C) Example movement traces with 400 ms feedback  
 111 delay. (D) Power spectra of cursor angular velocity with different feedback delays between 0–400 ms.  
 112 Average of 8 subjects, shading indicates standard error of mean (s.e.m.). See also Figure S2. (E)  
 113 Submovement periods (reciprocal of the peak frequency for each harmonic) for all subjects with  
 114 different feedback delays. See also Table S1. (F) Schematic of a simple delayed feedback controller.  
 115 (G) Amplitude response of the system shown in (F), known as a comb filter.

116 **Figure 1—source data 1.** This spreadsheet contains the frequencies of spectral peaks and associated  
 117 regression analysis shown in Figure 1D,E. These data can be opened with Microsoft Excel or with open-  
 118 source alternatives such as OpenOffice.

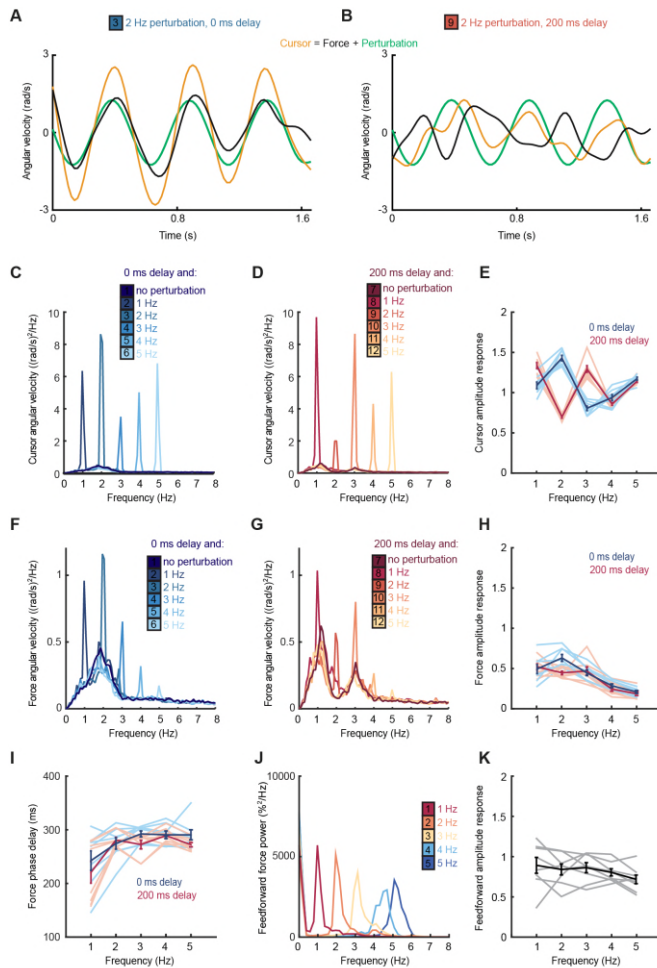
119 Figure 2A shows example tracking behavior with a 2 Hz perturbation. Note that the peak angular  
120 velocity of force responses (*black line*, calculated from the subject's finger forces) occurred around  
121 the same time as the peak angular velocity of the perturbation (*green line*). As a result, the angular  
122 velocity of the cursor (*yellow line*, reflecting the combination of the subject's forces with the  
123 perturbation) exhibited pronounced oscillations that were larger than the perturbation. Figure 2B  
124 shows performance in the same task when visual feedback was delayed by 200 ms. In this condition,  
125 peaks in force velocity coincided with perturbation troughs, attenuating the disturbance to cursor  
126 velocity. Figure 2C,D and Figure S3 overlay cursor velocity spectra in the presence of each perturbation  
127 frequency (with feedback delays of 0 and 200 ms). As previously, in the absence of feedback delay the  
128 frequency of submovements was around 2 Hz. Correspondingly, perturbations at 2 Hz induced a large  
129 peak in the cursor velocity spectrum, indicating that the artificial error was not effectively tracked. By  
130 contrast, with a feedback delay of 200 ms the cursor velocity spectrum with a 2 Hz perturbation was  
131 attenuated. The largest spectral peaks were instead associated with 1 and 3 Hz perturbations,  
132 matching the frequencies of submovements in this delay condition. Figure 2E shows the amplitude  
133 response of cursor movements (the relative amplitude of cursor movements phase-locked to the  
134 perturbation) at each frequency for both delay conditions. Cursor amplitude responses greater than  
135 unity at 2 Hz (with no delay), and at 1 and 3 Hz (with 200 ms delay) indicate exacerbation of  
136 intermittencies introduced by artificial errors at submovement frequencies. Analysis of variance  
137 (ANOVA) with two factors (delay time and perturbation frequency) revealed a highly significant  
138 interaction ( $n=8$  subjects,  $F_{4,70}=110.2$ ,  $P<0.0001$ ), confirming the interdependence of feedback delays  
139 and frequencies of constructive/destructive interference.

#### 140 *Feedback responses reflect filtered visual discrepancies*

141 It is clear from the velocity spectra in Figure 1D that not all submovement harmonics predicted by the  
142 comb filter model were present with the same amplitude within our tracking data. Rather,  
143 intermittency peaks for each delay condition were embedded within a broad low-pass envelope. Next  
144 we considered the origin of this delay-independent envelope. Our first hypothesis was that this might  
145 reflect the spectral content of motor noise during tracking. However we could reject this as the sole  
146 contributing factor by examining the force amplitude response to perturbations (the relative  
147 amplitude of force responses phase-locked to the perturbation). Figures 2F,G and Figure S4 show  
148 power spectra of the angular velocity derived from subject's forces, under feedback delays of 0 and  
149 200 ms. Figure 2H shows the corresponding force amplitude response at each frequency. Analyzed in  
150 this way, amplitude responses were largely independent of extrinsic delay. However, as with  
151 submovement peaks, feedback responses were also attenuated at higher frequencies. A two-factor  
152 ANOVA confirmed a significant main effect of frequency ( $n=8$  subjects,  $F_{4,70}=36.3$ ,  $P<0.0001$ ) but not  
153 delay time ( $F_{1,70}=3.1$ ,  $P=0.08$ ), and only a weakly significant interaction ( $F_{4,70}=2.9$ ,  $P=0.03$ ). Moreover,  
154 the phase delay of force responses was reduced at low frequencies (Fig. 2I). As with the amplitude  
155 response, there was a significant effect of frequency ( $F_{4,70}=9.5$ ,  $P<0.0001$ ) but not extrinsic delay ( $F_{1,70}$   
156  $=2.6$ ,  $P=0.12$ ) on this phase delay, and no significant interaction ( $F_{4,70}=0.7$ ,  $P=0.6$ ). In other words,  
157 feedback corrections to artificial noise with equal amplitude at different frequencies revealed  
158 characteristic signatures of a filter that was independent of extrinsic feedback delays. Moreover, this  
159 intrinsic filter had the appropriate bandwidth to account for attenuation of intermittency at higher  
160 frequencies.

161





162

163 **Figure 2. Frequency responses and phase delays to artificial motor errors.** (A) Example force (*black*)  
 164 and cursor (*yellow*) angular velocity traces in the presence of a 2 Hz perturbation (*green*). No feedback  
 165 delay is added. The force response and perturbation sum to produce large fluctuations in cursor  
 166 velocity. (B) Comparable data with a feedback delay of 200 ms. In this condition, force responses  
 167 cancel the perturbation leading to an attenuation of intermittency. (C) Power spectra of cursor angular  
 168 velocity with 1–5 Hz perturbations and no feedback delay. Average of 8 subjects. See also Figure S3.  
 169 (D) Power spectra of cursor angular velocity with 1–5 Hz perturbations and 200 ms feedback delay.  
 170 (E) Cursor amplitude response to 1–5 Hz perturbations with no feedback delay (*blue*) and 200 ms  
 171 feedback delay (*red*) for individual subjects. Also shown is average  $\pm$  s.e.m. of 8 subjects. (F) Power  
 172 spectra of force angular velocity with 1–5 Hz perturbations and no feedback delay. See also Figure S4.  
 173 (G) Power spectra of force angular velocity with 1–5 Hz perturbations and 200 ms feedback delay. (H)  
 174 Force amplitude response to 1–5 Hz perturbations with no feedback delay (*blue*) and 200 ms feedback  
 175 delay (*red*). Also shown is average  $\pm$  s.e.m. of 8 subjects. (I) Intrinsic phase delay of force response to  
 176 1–5 Hz perturbations with no feedback delay (*blue*) and 200 ms feedback delay (*red*). Also shown is  
 177 average  $\pm$  s.e.m. of 8 subjects. (J) Power spectrum of finger forces generated in the feedforward task  
 178 with auditory cues at 1-5 Hz. Average of 8 subjects. See also Figure S5. (K) Force amplitude response  
 179 to auditory cues in the feedforward task. Also shown is average  $\pm$  s.e.m. of 8 subjects.

180 **Figure 2—source data 2.** This spreadsheet contains the cursor/force/feedforward amplitude response  
 181 and phase delay data shown in Figure 2E,H,I,K. These data can be opened with Microsoft Excel or with  
 182 open-source alternatives such as OpenOffice.

183 Next we considered whether this attenuation was a property of motor pathways, for example  
 184 reflecting filtering by the musculoskeletal system. However, it is well-known that the frequencies of  
 185 feedforward movements can readily exceed submovement frequencies observed during feedback-  
 186 guided behavior (Kunesch *et al.*, 1989). We confirmed this by asking subjects to produce force  
 187 fluctuations of a defined amplitude, but without providing a moving target to track. Instead we used  
 188 auditory cues (a metronome) to indicate the required movement frequency. In this case, subjects  
 189 could generate force fluctuations up to 5 Hz with little attenuation (Fig. 2J,K and Fig. S5). Therefore  
 190 we concluded that filtering during visuomotor tracking was not inherent to the motor pathway and  
 191 considered instead whether it could be a property of the feedback loop.

192

### 193 *Filtered feedback corrections are consistent with optimal state estimation*

194 The visual system can perceive relatively high frequencies (up to flicker-fusion frequencies above 10  
 195 Hz). However, for movements in the physical world, it is unlikely that high-frequency tracking  
 196 discrepancies reflect genuine motor errors, since this would imply implausibly large accelerations of  
 197 the body. Given inherent uncertainties in sensation, an optimal state estimator should attribute such  
 198 errors to sensory noise (as this is unconstrained by Newtonian dynamics). Formally, the task of  
 199 distinguishing the true state of the world from uncertain, delayed measurements can be achieved by  
 200 a Kalman filter which continuously integrates new evidence with updated estimates of the current  
 201 state evolving according to a model of the external dynamics (Fig. 3A). For simplicity we assumed the  
 202 1D position of the body (cursor) should move with constant velocity relative to the slow, predictable  
 203 target unless acted upon by accelerative forces, leading to a two-dimensional state transition model:

$$204 \quad \begin{bmatrix} x_k \\ v_k \end{bmatrix} = \begin{bmatrix} 1 & \Delta t \\ 0 & 1 \end{bmatrix} \begin{bmatrix} x_{k-1} \\ v_{k-1} \end{bmatrix} + \begin{bmatrix} 0 \\ \Delta t \end{bmatrix} a_k \quad (\text{Equ. 2})$$

205 where  $x_k$  and  $v_k$  are the relative position and velocity of the cursor at time-step  $k$ ,  $\Delta t$  is the interval  
 206 between time-steps, and the process noise  $a_k \sim N(0, \sigma_a^2)$ . Visual feedback,  $y_k$ , was assumed to  
 207 comprise a noisy measurement of relative position:

$$208 \quad y_k = x_k + \varepsilon_k \quad (\text{Equ. 3})$$

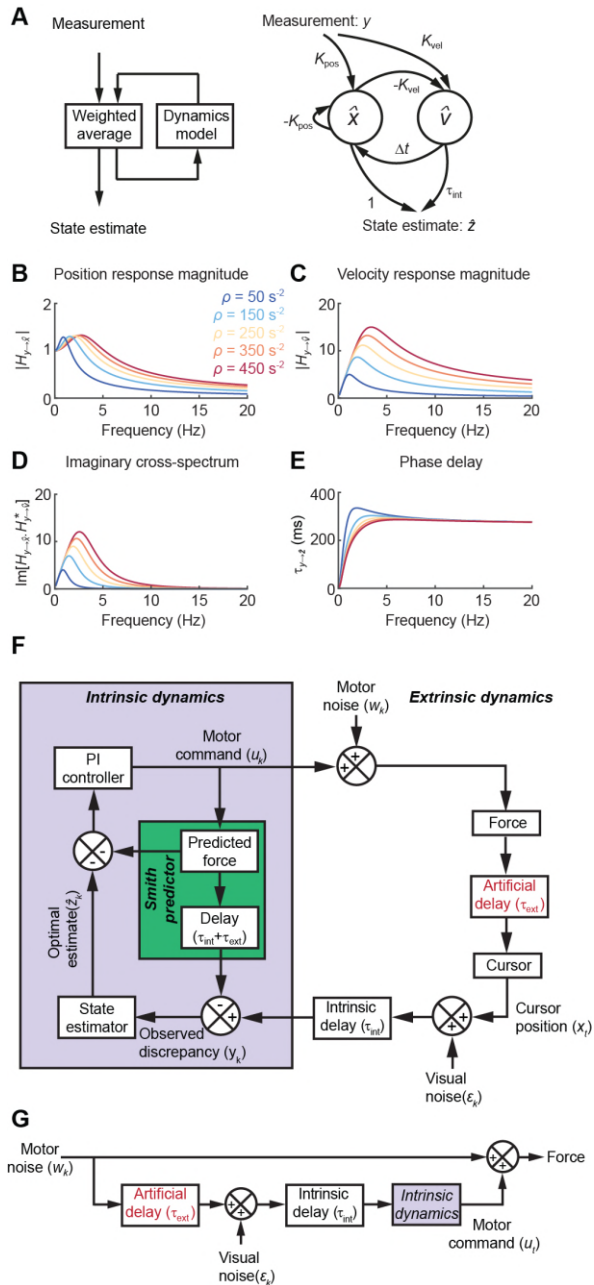
209 with measurement noise  $\varepsilon_k \sim N(0, \sigma_\varepsilon^2)$ . Optimal estimates of relative position and velocity,  $\hat{x}_k$  and  $\hat{v}_k$   
 210 are given by a steady-state Kalman filter of the form:

$$211 \quad \begin{bmatrix} \hat{x}_k \\ \hat{v}_k \end{bmatrix} = \begin{bmatrix} 1 - K_{\text{pos}} & \Delta t \\ -K_{\text{vel}} & 1 \end{bmatrix} \begin{bmatrix} \hat{x}_{k-1} \\ \hat{v}_{k-1} \end{bmatrix} + \begin{bmatrix} K_{\text{pos}} \\ K_{\text{vel}} \end{bmatrix} y_{k-1} \quad (\text{Equ. 4})$$

212 The innovation gains  $K_{\text{pos}}$  and  $K_{\text{vel}}$  depend only on the ratio of process to measurement noise,  $\rho =$   
 213  $\sigma_a/\sigma_\varepsilon$ , which in turn determines the cut-off frequency above which measurements are filtered  
 214 ( $2\pi f \sim \sqrt{\rho}$ ). Figure 3B,C shows the amplitude response for position and velocity estimates. Note that  
 215 these are out of phase with each other, and therefore broadband input results in a complex cross-  
 216 spectral density between them. The imaginary component of this cross-spectrum exhibits a  
 217 characteristic resonance peak (Fig. 3D). Feedback delays can be accommodated by projecting the state  
 218 estimate forward in time:

$$219 \quad \hat{z}_k = \begin{bmatrix} 1 & \tau_{\text{int}} \end{bmatrix} \begin{bmatrix} \hat{x}_k \\ \hat{v}_k \end{bmatrix} \quad (\text{Equ. 5})$$

220



221

222

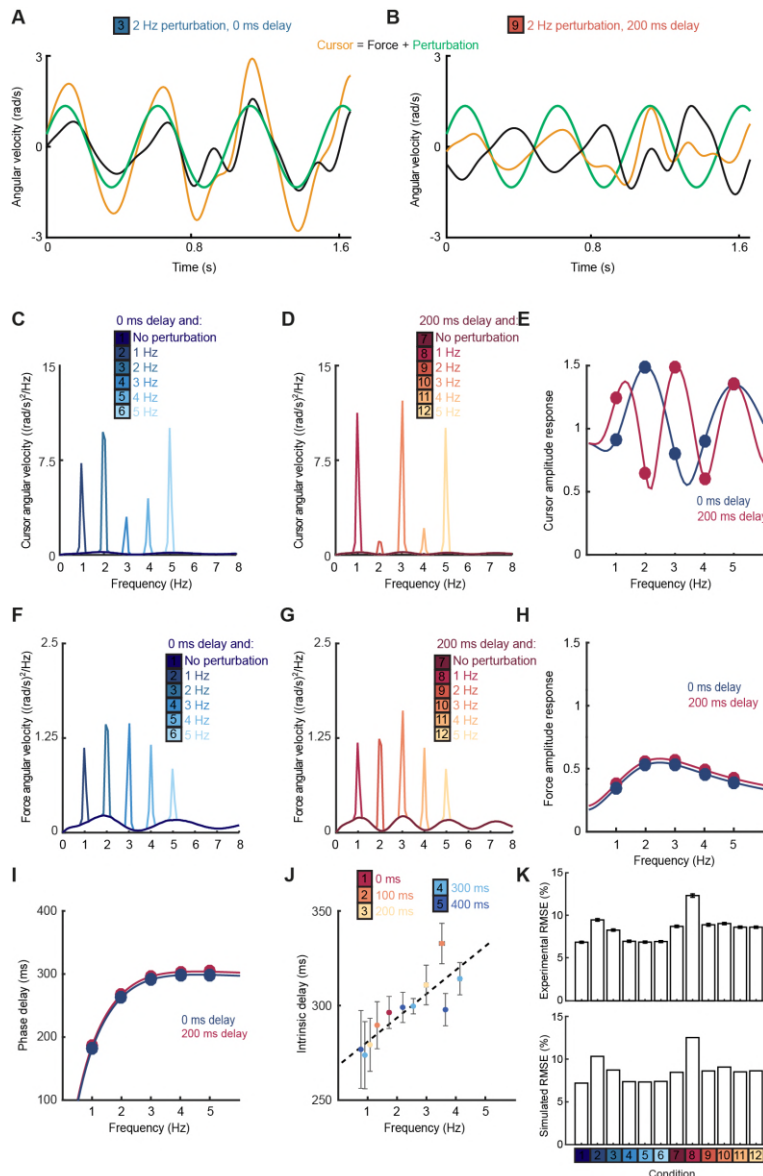
223 **Figure 3. State estimation with a Kalman filter.** (A) *Left*: Schematic of a Kalman filter. Noisy  
 224 measurements are combined with an internal model of the external dynamics to update an optimal  
 225 estimate of current state. *Right*: A dynamical system for optimal estimation of position, based on an  
 226 internal model of position and velocity. (B, C) Magnitude response of transfer function from  
 227 measurement to position and velocity estimates for the Kalman filter with different ratios of process  
 228 to measurement noise ( $\rho$ ). (D) Imaginary component of cross-spectrum between position and velocity  
 229 transfer functions. (E) Phase delay of optimal estimate of position based on delayed measurement of  
 230 position. (F) Schematic of optimal feedback controller model incorporating state estimation and a  
 231 Smith Predictor architecture to accommodate feedback delays. (G) Simplified rearrangement of (F),  
 232 showing the feedforward relationship between motor noise and force output. This rearrangement is  
 233 possible because the Smith Predictor prevents motor corrections reverberating multiple times around  
 234 the feedback loop.

235 The phase delay of the optimal position estimate for the current state,  $\hat{z}_k$ , falls towards zero at low  
236 frequencies, consistent with successful prediction on the basis of delayed measurement (Fig. 3E). This  
237 steady-state Kalman filter was incorporated within a 1D feedback controller (Fig. 3F; see Methods for  
238 details) which also included an internal feedback loop to cancel the sensory consequences of motor  
239 commands. This architecture, known as a Smith Predictor (Miall *et al.*, 1993b; Abe and Yamanaka,  
240 2003), prevents corrections from reverberating around the external feedback loop, such that the  
241 resultant closed-loop behavior is formally equivalent to the simpler feedforward system shown in  
242 Figure 3G. This rearrangement provides a useful intuition about our behavioral results. Tracking errors  
243 (due to motor noise) drive feedback corrections that are delayed, corrupted (by sensory noise) and  
244 filtered (by intrinsic dynamics). The power spectrum of the resultant movement reflects  
245 constructive/destructive interference between feedback corrections and the original tracking error.

246 This simple model readily accounted for the main features of our human data, including the cursor  
247 amplitude response to perturbations (Fig. 4A-E), and the low-pass filtering (Fig. 4F-H) and phase delay  
248 (Fig. 4I) of force responses. Moreover, because of frequency-dependent phase delays introduced by  
249 state estimation, the model predicted that precise frequencies of submovement peaks should deviate  
250 slightly from those calculated using a constant physiological response latency. This effect was  
251 confirmed in our behavioral data by calculating (with Equ. 1) the intrinsic delay time corresponding to  
252 each spectral harmonic under all feedback delays (Fig. 1D). This intrinsic delay time was positively  
253 correlated with the frequency of the harmonic (n=11 spectral peaks, R=0.85, P=0.0009; Fig. 4J). Finally,  
254 overall tracking performance (as measured by the root mean squared positional error over time)  
255 matched well with subjects' actual performance across conditions (Fig. 4K). Note that irrespective of  
256 delay, the lowest frequency perturbation was associated with the greatest positional error (since  
257 perturbations had equal peak-to-peak velocity and were therefore larger in amplitude at low  
258 frequencies). However, performance was most affected by the 1 Hz perturbation with a 200 ms delay,  
259 corresponding to a frequency of constructive interference.

260 In summary, amplitude and phase responses to perturbations during human visuomotor tracking  
261 provide compelling evidence for intrinsic filtering of measurement noise from feedback corrections,  
262 while a plausible computational justification is provided by optimal state estimation. Moreover, while  
263 this interpretation is derived from computational principles, the schematic on the right of Fig. 3A  
264 suggests how a steady-state Kalman filter could be implemented by neural circuitry. Two neural  
265 populations representing position and velocity should evolve according to Equ. 4 and thus exhibit a  
266 resonance peak in their imaginary cross-spectrum. To seek further evidence for the neural  
267 implementation of such a filter we turned to intracortical recordings in non-human primates.

268



269

270 **Figure 4. OFC model reproduces human behavioral data.** (A) Simulated tracking performance of the  
 271 OFC model with a 2 Hz sinusoidal perturbation and no feedback delay. (B) Simulated tracking  
 272 performance of the OFC model with a 2 Hz sinusoidal perturbation and 200 ms feedback delay. (C)  
 273 Power spectrum of simulated cursor velocity with 1–5 Hz perturbations and no feedback delay. (D)  
 274 Power spectrum of simulated cursor velocity with 1–5 Hz perturbations and 200 ms feedback delay.  
 275 (E) Simulated cursor amplitude response to 1–5 Hz perturbations with no feedback delay (*blue*) and  
 276 200 ms feedback delay (*red*). (F) Power spectrum of simulated force velocity with 1–5 Hz perturbations  
 277 and no feedback delay. (G) Power spectrum of simulated force velocity with 1–5 Hz perturbations and  
 278 200 ms feedback delay. (H) Simulated force amplitude response to 1–5 Hz perturbations with no  
 279 feedback delay (*blue*) and 200 ms feedback delay (*red*). (I) Simulated intrinsic phase delay of force  
 280 responses to 1–5 Hz perturbations with no feedback delay (*blue*) and 200 ms feedback delay (*red*). (J)  
 281 Intrinsic delay times corresponding to all submovement peaks/harmonics in Figure 1D, plotted against  
 282 the frequency of the peak. Error bars indicate s.e.m. across 8 subjects. (K) *Top*: Positional inaccuracy  
 283 of human tracking for all conditions quantified as root mean squared error (RMSE). Average  $\pm$  s.e.m.  
 284 of 8 subjects. *Bottom*: RMSE of simulated tracking for all conditions.

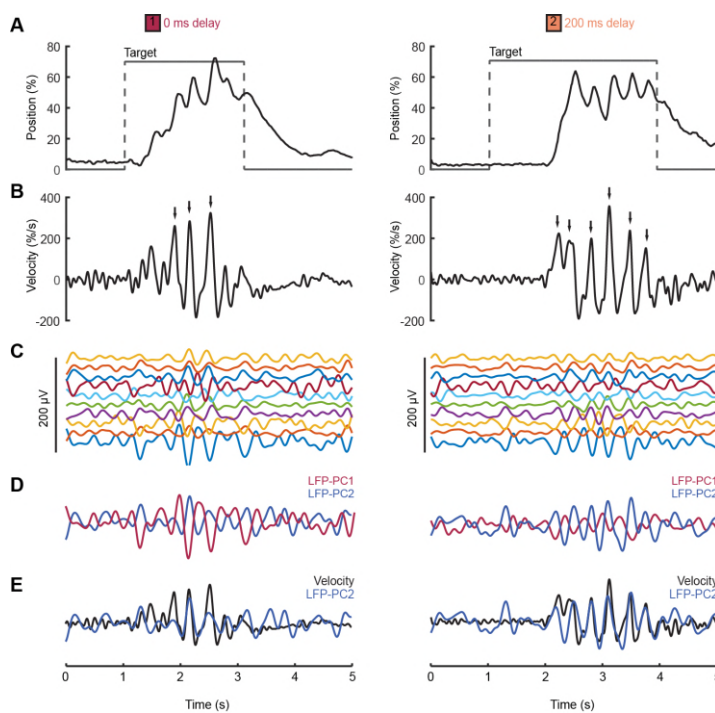
285



286 *Movement intermittency in a non-human primate tracking task*

287 We were interested in whether cyclical motor cortex dynamics could reflect the neural correlates of  
288 the two interacting neural populations described above, and thereby account for filtering of feedback  
289 responses during visuomotor tracking. We therefore analyzed local field potential (LFP) recordings  
290 from monkey primary motor cortex (M1) during a center-out isometric wrist torque task that we have  
291 used previously to characterize both submovement kinematics and population dynamics (Hall *et al.*,  
292 2014). Figure 5 shows example tracking behavior (Fig. 5A), radial cursor velocity (Fig. 5B) and  
293 multichannel LFPs (Fig. 5C) as monkeys moved to peripheral targets under two feedback delay  
294 conditions. Movement intermittency was apparent as regular submovement peaks in the radial cursor  
295 velocity. Moreover LFPs exhibited low-frequency oscillations during movement, with a variety of  
296 phase-shifts present on different channels. Principal component analysis (PCA) yielded two orthogonal  
297 components of the cortical cycle (Fig. 5E), and the close coupling with submovements was revealed  
298 by overlaying the cursor velocity profile onto, in this case, the second principal component (PC) (Fig.  
299 5E).

300



301

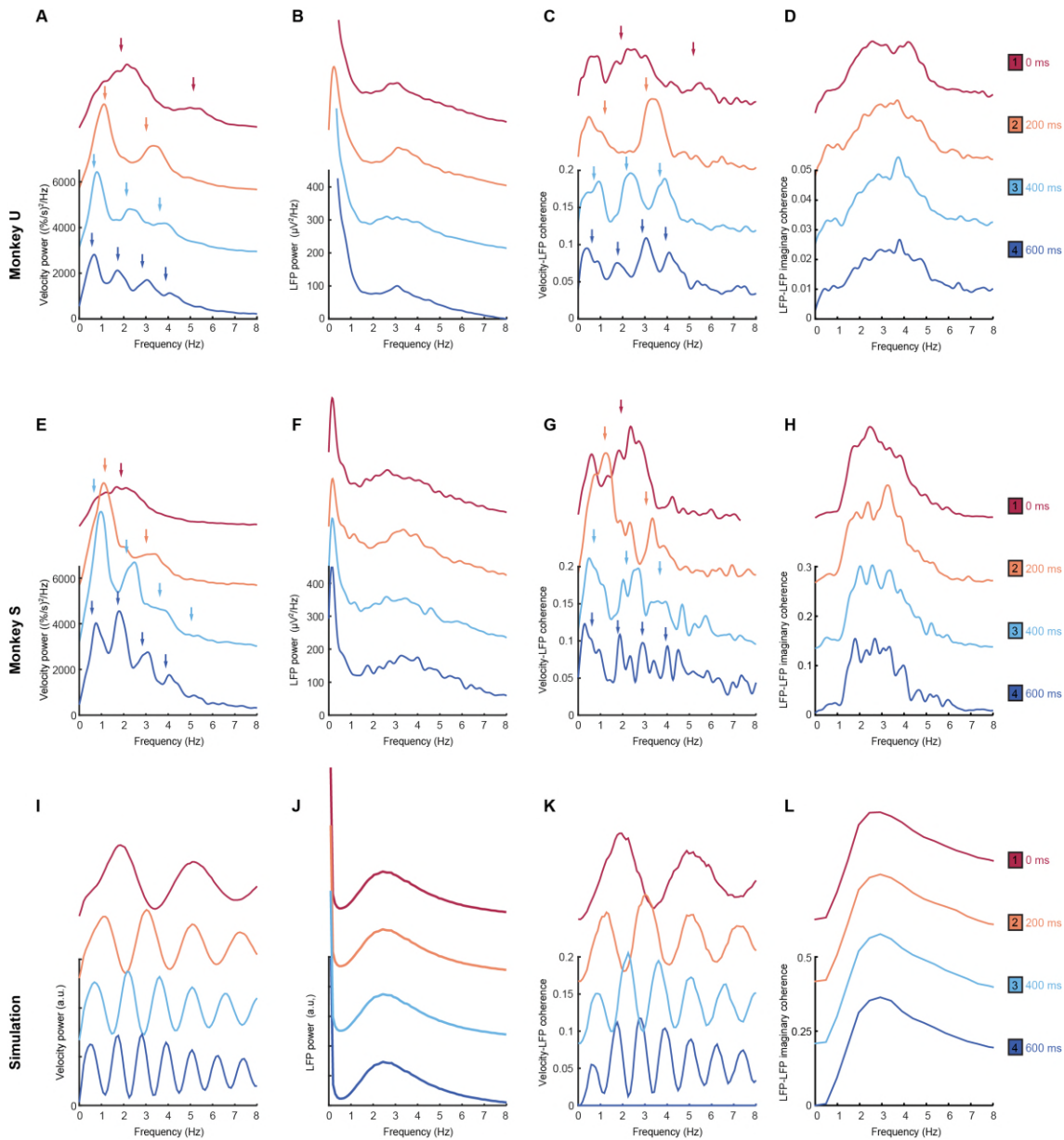
302 **Figure 5. Movement intermittency in a non-human primate tracking task.** (A) Radial cursor position  
303 during a typical trial of the center-out isometric wrist torque task under two different feedback delay  
304 conditions. Data from Monkey U. (B) Radial cursor velocity. Arrowheads indicate time of  
305 submovements identified as positive peaks in radial cursor velocity >150%/s. (C) Low-pass filtered,  
306 mean-subtracted LFPs from M1. (D) First two principal components (PCs) of the LFP. (E) The second  
307 LFP-PC overlaid on the radial cursor velocity.

308

309 As with humans, in the absence of feedback delay the cursor velocity (after removing task-locked  
310 components, see Methods) was dominated by a single spectral peak around 2-3 Hz (Fig. 6A,E; *top*  
311 *red traces*). A broad peak at approximately the same frequency was also observed in average LFP  
312 power spectra (Fig. 6B,F), while coherence analysis confirmed consistent phase-coupling between

313 LFPs and cursor velocity (Fig. 6C,G). We also calculated imaginary coherence spectra between pairs  
 314 of LFPs (see Methods) to separate local signal components with a consistent, non-zero phase  
 315 difference from in-phase components (e.g. due to volume conduction from distant sources), which  
 316 revealed more clearly the 2-3 Hz LFP oscillation (Fig. 6D,H). An obvious interpretation of these  
 317 results could be that oscillatory activity in the motor system drives submovements in a feedforward  
 318 manner. In this case we would expect the frequency of the cortical oscillation to reliably reflect the  
 319 intermittency observed in behavior.

320



321

322 **Figure 6. Frequency-domain analysis reveals delay-dependent and delay-independent spectral**  
 323 **features.** (A) Power spectrum of radial cursor speed with 0–600 ms feedback delay. Traces have been  
 324 off-set for clarity. Arrows indicate expected frequencies of peaks from OFC model. Data from Monkey  
 325 U. (B) Average power spectrum of M1 LFPs. (C) Average coherence spectrum between radial cursor  
 326 speed and all M1 LFPs. (D) Average imaginary coherence spectrum between all pairs of M1 LFPs. (E-  
 327 H) As above, but for Monkey S. (I-L) Simulated power and coherence spectra produced by the OFC  
 328 model.

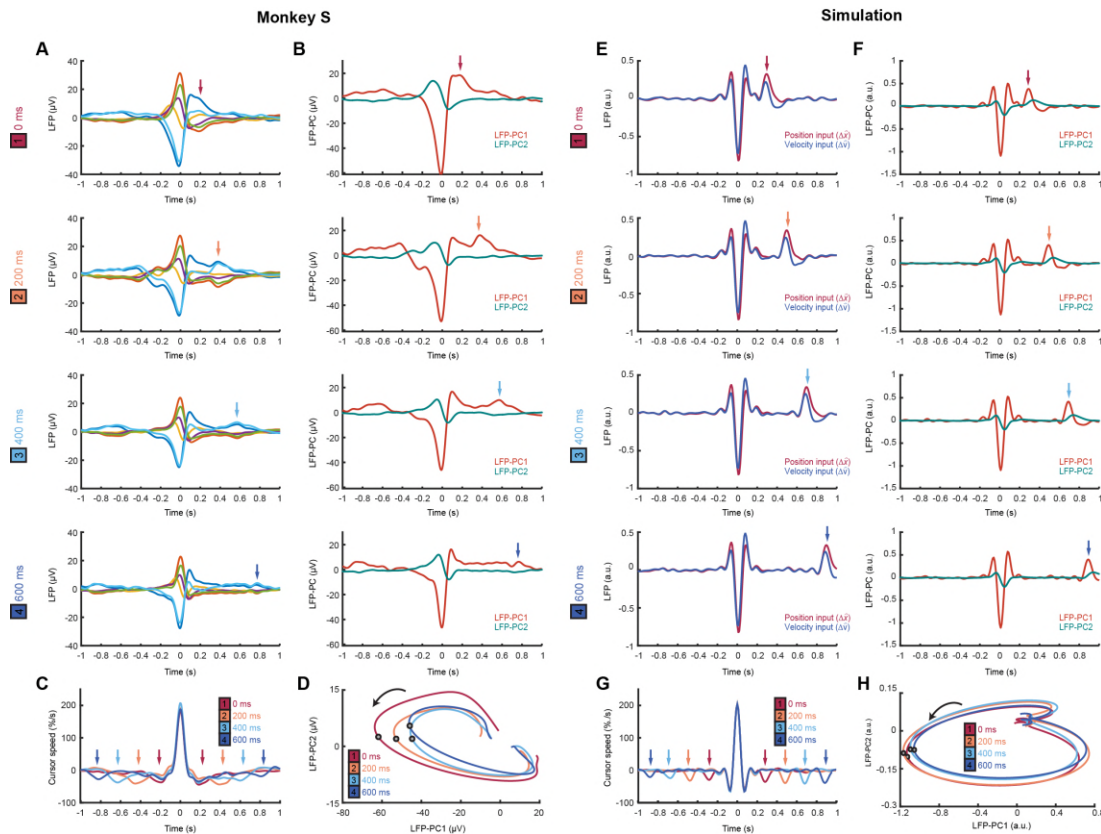
329 *Feedback delays dissociate intrinsic and extrinsic contributions to intermittency*

330 With increasing feedback delays, submovement peaks in monkeys (Fig. 6A,E) exhibited a pattern  
331 similar to that seen with human subjects. The fundamental frequency was reduced, while odd  
332 harmonics grew more pronounced as they came below about 4 Hz. Moreover, coherence spectra  
333 between cursor velocity and LFP (Fig. 6C,G) revealed peaks at both fundamental and harmonic  
334 frequencies. Surprisingly however, the power spectrum of the LFP (Fig. 6B,F) was unaffected by  
335 feedback delay, with a single broad peak in the delta band persisting throughout. Moreover, imaginary  
336 coherence spectra between pairs of LFPs were also unchanged (Fig. 6D,H). These results appear  
337 incompatible with the hypothesis that motor cortical oscillations drive movement intermittency, and  
338 instead demonstrate a dissociation between delay-dependent submovements and the conserved  
339 rhythmicity of LFPs.

340 We next identified submovements from peaks in the radial cursor speed, in order to examine the  
341 temporal profile of their associated LFPs. Submovement-triggered averages (SmTAs) of LFPs exhibited  
342 multiphasic potentials around the time of movement, as well as a second feature following  
343 submovements with a latency that depended on extrinsic delay (Fig. 7A, Fig. S6A). This feature was  
344 revealed more clearly by reducing the dimensionality of the LFPs with PCA (Fig. 7B, Fig. S6B). Note that  
345 if submovements reflect interference between stochastic motor errors and feedback corrections, a  
346 submovement in the positive direction can arise from two underlying causes. First, it may be a positive  
347 correction to a preceding negative error. In this case, cortical activity associated with the feedback  
348 correction should occur around time zero. Second, the submovement may itself be a positive error  
349 which is followed by a negative correction, and the associated cortical activity will hence be delayed  
350 by the feedback latency. Since the SmTA pools submovements arising from both causes, this accounts  
351 for two features with opposite polarity separated by the feedback delay. Note also that SmTAs of  
352 cursor velocity similarly overlay (negative) tracking errors preceding (positive) feedback corrections,  
353 and (negative) feedback corrections following (positive) tracking errors, evident as symmetrical  
354 troughs on either side of the central submovement peak (Fig. 7C, Fig. S6C).

355 Importantly however, LFP oscillations around the time of submovements appeared largely unaffected  
356 by delay. To visualize this, we projected the SmTAs of multichannel LFPs onto the same PC plane. For  
357 all delay conditions, LFPs traced a single cycle with the same directional of rotation and comparable  
358 angular velocity (Fig. 7D, Fig. S6D). The period of these cycles (approx. 300 ms) matched the frequency  
359 of imaginary coherence between LFPs (approx. 3 Hz), as expected since signals with a consistent phase  
360 difference will be orthogonalized by PCA and appear as cyclical trajectories in the PC plane. In other  
361 words, although the precise frequency of submovements depends on extrinsic delays in visual  
362 feedback, the constant frequency of associated LFP cycles reveals conserved intrinsic dynamics within  
363 population activity in the motor cortex. Note also that the resonant frequency of these dynamics  
364 matches the intrinsic filtering of feedback responses observed in our human experiments.

365



366

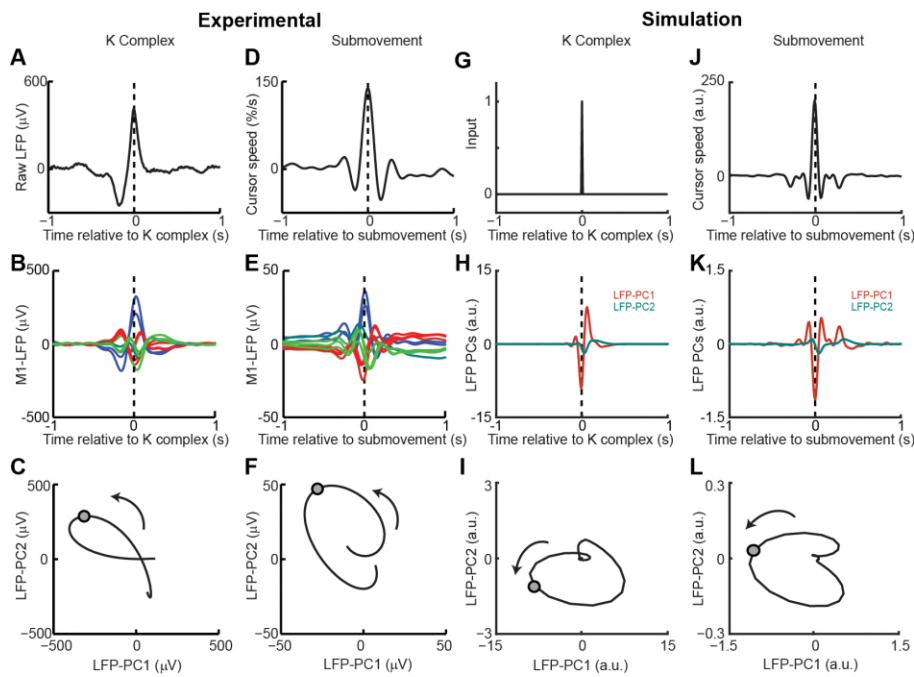
367 **Figure 7. Submovement-triggered averages of M1 LFPs.** (A) Average low-pass filtered LFPs from M1,  
 368 aligned to the peak speed of submovements with 0–600 ms feedback delay. Arrows indicate second  
 369 feature following submovement by an extrinsic delay-dependent latency. Data from Monkey S. See  
 370 also Figure S6. (B) Average of first two LFP-PCs aligned to submovements. (C) Average low-pass filtered  
 371 cursor speed, aligned to submovements. Arrows indicate symmetrical velocity troughs at extrinsic  
 372 delay-dependent latencies. (D) Average submovement-triggered LFP-PC trajectories, plotted over 200  
 373 ms either side of the time of peak submovement speed (indicated by circles). (E-H) Simulated  
 374 submovement-triggered averages produced by the OFC model.

375

### 376 *Modelling submovement-related LFP cycles and delta oscillations in sleep*

377 These various observations can be understood using the same computational model that explained  
 378 our human behavioral data (Figure S7). For simplicity, we simulated two out-of-phase components  
 379 within the LFP from the total synaptic input to each of the two neural population in the state  
 380 estimator. We also added common low-frequency background noise to represent volume conduction  
 381 from distant sources. The simulated LFPs exhibited a broad (delay-independent) spectral peak arising  
 382 from the dynamics of the recurrent network (Fig. 6J). By contrast, the resultant cursor velocity  
 383 comprised the summation of motor noise and (delayed) feedback corrections, and therefore  
 384 contained sharper (delay-dependent) spectral peaks due to constructive/destructive interference (Fig.  
 385 6I). Note however that coherence was nonetheless observed between LFPs and cursor velocity (Fig.  
 386 6K). Time-domain SmTAs of the simulated data also reproduced features of the experimental  
 387 recordings, including delay-dependent peaks/troughs reflecting extrinsic feedback delays (Fig. 7E-G).  
 388 Meanwhile, the conserved intrinsic dynamics coupling simulated neural populations resulted in  
 389 consistent cyclical LFP trajectories around the time of movement (Fig. 7H) and an imaginary cross-  
 390 spectrum with a single delay-independent resonance (Fig. 6L).





391  
392

393 **Figure 8. Simulated LFP dynamics during movement and sedation.** (A) K-complex events in LFP from  
394 M1 recorded under ketamine sedation. (B) Average low-pass filtered multichannel LFPs aligned to K-  
395 complex events. LFPs are color-coded according to phase relative to submovements, but exhibit a  
396 similar pattern relative to K complexes. (C) Average LFP-PC trajectories aligned to K-complexes,  
397 plotted over 200 ms either side of the time of K-complex (indicated by circle), using the PC plane  
398 calculated from recordings during awake behavior. (D) Average cursor speed aligned to the peak speed  
399 of submovements. (E) Average low-pass filtered multichannel LFPs aligned to submovements. (F)  
400 Average submovement-triggered LFP-PC trajectories, plotted over 200 ms either side of the time of  
401 submovements (indicated by circle). (G) A K-complex under sedation is simulated by an impulse  
402 excitation of the OFC model, without connection to the external world. (H) Impulse response of the  
403 simulated LFP-PCs. (I) LFP-PC trajectories associated with simulated K-complexes. (J) Simulated  
404 submovement-triggered average cursor speed from the OFC model with no feedback delay. (K)  
405 Simulated submovement-triggered average LFP-PCs. (L) Simulated submovement-triggered LFP-PC  
406 trajectories. Panels A-F reproduced from Figure 4A,C,D in Hall et al. (2014) under the CC BY 3.0 license  
407 (<https://creativecommons.org/licenses/by/3.0/>).

408

409 Finally we examined whether the model could also account for cortical oscillations in the absence of  
410 behavior. Previously we have described a common dynamical structure within both cortical cycles  
411 during movement and low-frequency oscillations during sleep and sedation (Hall *et al.*, 2014). In  
412 particular, K-complex events under ketamine sedation (Fig. 8A), thought to reflect transitions between  
413 down- and up-states of the cortex, are associated with brief bursts of delta oscillation (Fig. 8B) (Amzica  
414 and Steriade, 1997). The relative phases of multichannel LFPs aligned to these events matches those  
415 seen during submovements (Fig. 8D,E). As a result, when projected onto the PC plane, LFPs trace  
416 similar cycles during both K-complexes (Fig. 8C) and submovements (Fig. 8F). We modelled the  
417 sedated condition by disconnecting motor and sensory connections between the feedback controller  
418 and the external world, instead providing a pulsatile input to the state estimator simulating a down-  
419 to up-state transition (Fig. 8G). Effectively, transient excitation of the state estimator elicited an  
420 impulse response reflecting its intrinsic dynamics. The simulated LFPs generated a burst of delta-



421 frequency oscillation around the K-complex (Fig. 8H) which resembled submovement-related activity  
422 (Fig. 8J,K). Projecting this activity onto the same PC plane revealed consistent cycles during simulated  
423 K-complexes (Fig. 8I) and submovements (Fig. 8L). Thus it appears that our computational model  
424 incorporating the intrinsic dynamics of motor cortical networks could also account for the conserved  
425 structure of low-frequency LFPs during movement and delta oscillations in sleep.

426

## 427 **Discussion**

### 428 *Submovement kinematics are influenced by both extrinsic and intrinsic dynamics*

429 Previous theories of intermittency have focused on either extrinsic or intrinsic explanations for the  
430 regularity of submovements, but little consensus has emerged over this fundamental feature of  
431 movement. There is good evidence for a common low-frequency oscillatory structure to motor cortex  
432 activity across multiple behavioral states (Churchland *et al.*, 2012; Hall *et al.*, 2014; Russo *et al.*, 2018)  
433 but also an influence of feedback delays on submovement timing (Miall, 1996). Experimentally  
434 manipulating visual feedback with artificial time delays and spatial perturbations allowed us to  
435 dissociate both contributions to submovement kinematics. We found that precise frequencies of  
436 submovement peaks were determined by constructive and destructive interference between broad-  
437 band motor errors and continuous, delayed feedback corrections. However, these peaks were  
438 embedded within a delay-independent envelope that arose from intrinsic filtering of feedback  
439 corrections. The dissociation of extrinsic and intrinsic dynamics was also evident in cortical LFPs during  
440 tracking movements. Both delay-dependent feedback corrections and delay-independent cycles were  
441 observed in submovement-triggered averages of LFPs. Moreover, while coherence between LFPs and  
442 cursor movement exhibited delay-dependent spectral peaks, the imaginary coherence between  
443 multichannel LFPs revealed a consistent dynamical structure across behaviors.

444 These apparently contradictory results could be explained by an OFC model that implemented state  
445 estimation via a steady-state Kalman filter to separate process (motor) noise from measurement  
446 (sensory) noise. One free parameter was tuned to achieve correspondence between simulated and  
447 experimental data, namely the ratio of process to measurement noise which determined the intrinsic  
448 resonance frequency around 2-3 Hz. It would be interesting in future to vary these noise  
449 characteristics experimentally (e.g. by artificially degrading visual acuity or by extensively training  
450 subjects) and examine the effect on perturbation responses. One possible outcome would be a change  
451 to the observed resonance, although this seems to contradict the ubiquity of 2-3 Hz cortical dynamics.  
452 Alternatively there may be other computational advantages to maintaining a consistent cortical  
453 rhythm. For example, it is notable that 2-3 Hz intrinsic dynamics matched the frequency of the primary  
454 submovement peak under unperturbed external feedback conditions, thus accentuating the  
455 fundamental submovement frequency around 2 Hz while suppressing higher harmonics. This may be  
456 beneficial in allowing other aspects of the visuomotor machinery to be synchronized to a single  
457 rhythm, for example eye movements which are influenced by hand movement during tracking tasks  
458 (Koken and Erkelens, 1992).

459

### 460 *Modelling isometric visuomotor tracking*

461 Several further assumptions of our modelling warrant discussion. First, to prevent control instabilities  
462 associated with feedback delays we incorporated an accurate forward model of the (delayed) sensory  
463 consequences of motor commands within a Smith Predictor architecture. We did not include adaptive

464 processes to calibrate the delay model, but this could be readily achieved by minimizing discrepancies  
465 between an efference copy of motor commands and observed cursor movements. The accuracy of  
466 tracking performance under different delay conditions (without cursor perturbations) suggests that  
467 subjects could readily adapt such a forward model and this role has previously been ascribed to the  
468 cerebellum (Miall *et al.*, 1993b; Streng *et al.*, 2018). By contrast, to account for the delay-independent  
469 perturbation responses, we maintained the same intrinsic cortical dynamics throughout, even though  
470 an optimal state estimator should similarly incorporate knowledge of feedback delays (see Equ. 5).  
471 Note however that adaptation of the state estimator presents a harder computational problem, since  
472 no available signals directly relate the state of the external world to delayed sensory information. Even  
473 when we imposed predictable sinusoidal perturbations, we saw no evidence that subjects learnt to  
474 compensate for feedback delays by altering the timing of their corrective responses within a single  
475 trial. Nevertheless, it would again be interesting to examine whether state estimator dynamics might  
476 adapt on a slower time-scale after extensive training with delayed feedback.

477 Finally, we were puzzled that force amplitude responses to cursor perturbations were uniformly less  
478 than unity, which initially appears suboptimal for rejecting even slow perturbations. We first  
479 considered that proprioceptive information (which is in conflict with vision during cursor  
480 perturbations) might cause subjects to underestimate the true displacement of the cursor. However,  
481 sub-unity amplitude responses were also observed in separate experiments (not shown) when  
482 sinusoidal displacements were added to the target position. In this situation there was no discrepancy  
483 between vision and proprioception, yet subjects consistently undershot corrections to all but the  
484 lowest frequency perturbations (even in the absence of any delay). In our OFC model we instead  
485 reduced amplitude responses by penalizing large changes to the motor command. This cost function  
486 was minimized by proportional-integral (PI) control, which has been used in the past to model human  
487 movement (Kleinman, 1974). It is more common in current optimal control models to apply cost  
488 functions that penalize the absolute motor command leading to proportional feedback policies  
489 (Todorov and Jordan, 2002), under the assumption that this minimizes signal-dependent noise in  
490 muscles (Jones *et al.*, 2002). However, the trajectory variability observed in our isometric tracking task  
491 appeared more correlated with large changes in finger forces rather than force magnitude (Figure S8),  
492 providing empirical support for our choice of cost function. Derivative-dependent motor noise was  
493 also evident as increased variability at high frequencies in our feedforward task (Figure S5). Since  
494 submovements result from constructive interference between tracking errors and feedback  
495 corrections, derivative-dependent motor noise also provides a counterintuitive but necessary  
496 explanation for why the amplitude of submovements increases with target speed (Figure S1).  
497 Increased intermittency cannot be a direct consequence of faster target motion, since the frequency  
498 content of this motion is nevertheless low by comparison to submovements. Rather, faster tracking  
499 requires a larger change in the motor command, leading to increased broad-band motor noise which,  
500 after constructive interference with feedback corrections, results in more pronounced peaks at  
501 submovement frequencies.

502

### 503 *State estimation by motor cortical population dynamics*

504 PCA of multichannel LFPs in monkey motor cortex revealed two underlying components, which we  
505 interpret as arising from distinct but coupled neural populations. The cyclical movement-related  
506 dynamics of these components resembled those described for M1 firing rates (Churchland *et al.*,  
507 2012), which have previously been implicated in feedforward generation of movement. Specifically, it  
508 was proposed that preparatory activity first develops along ‘output-null’ dimensions of the neural  
509 state space before, at movement onset, evolving via intrinsic dynamics into orthogonal ‘output-

510 potent' dimensions that drive muscles (Churchland *et al.*, 2010). However, this purely feedforward  
511 view cannot account for our isometric tracking data, since manipulation of feedback delays dissociated  
512 delay-dependent submovements from delay-independent rotational dynamics. Instead we interpret  
513 these intrinsic dynamics as implementing a state estimator during continuous feedback control. We  
514 used Newtonian dynamics to construct a simple two-dimensional state transition model based on  
515 both the cursor-target discrepancy and its first derivative. While this undoubtedly neglects the true  
516 complexity of muscle and limb biomechanics, simulations based on this plausible first approximation  
517 reproduced both the amplitude response and phase delay to sinusoidal cursor perturbations in  
518 humans, and the population dynamics of LFP cycles in the monkey. Note that this account also offers  
519 a natural explanation of why preparatory and movement-related activity lies along distinct state-space  
520 dimensions, since the static discrepancy present during preparation is encoded differently to the  
521 changing discrepancy that exists during movement. At the same time, the lawful relationship between  
522 discrepancy and its derivative couples these dimensions within the state estimator and is evident as  
523 consistent rotational dynamics across different tasks and behavioral states.

524 It may seem unusual to ascribe the role of state estimation to M1 when this function is usually  
525 attributed to parietal (Mulliken *et al.*, 2008) and premotor areas (where rotational dynamics have also  
526 been reported, albeit at a lower frequency (Churchland *et al.*, 2012; Hall *et al.*, 2014). We suggest that  
527 the computations involved in optimal visuomotor tracking are likely distributed across multiple  
528 cortical areas including (but not limited to) M1, with local circuitry reflecting multiple dynamical  
529 models of the various sensory and efference copy signals that must be integrated for accurate control.  
530 Indeed, while we neglected to model the computations involved in accurately estimating our slow and  
531 predictable target motion, state estimation using Kalman filters has also been suggested as a  
532 mechanism by which the visual system can estimate the position of moving visual stimuli (Kwon *et al.*,  
533 2015).

534 An alternative explanation for consistent rotational dynamics has recently been proposed by Russo *et al.*  
535 (2018), based on the behavior of recurrent neural networks trained to produce different feed-  
536 forward muscle patterns whilst minimizing 'tangling' between neural trajectories. It is interesting to  
537 compare this with our OFC-based interpretation, since both are motivated by the problem of  
538 maintaining accurate behavior in the presence of noise. Minimizing tangling leads to network  
539 architectures that are robust to intrinsic noise in individual neurons, while OFC focusses on optimizing  
540 movements in the face of unreliable motor commands and noisy sensory signals. Given this conceptual  
541 link, it is perhaps unsurprising if recurrent neural network approaches learn implementations of  
542 computational architectures such as Kalman filters that minimize the influence of noise on behavior.  
543 In future it may be productive to incorporate sensory feedback into recurrent neural network models  
544 of movement, as well as including intrinsic sources of neural noise in optimal control models. The  
545 convergence of these frameworks may further help to reveal how computational principles are  
546 implemented in the human motor system.

547

## 548 **Acknowledgements**

549 We thank Jenifer Tulip and Norman Charlton for technical assistance. This work was supported by  
550 the Indonesia Endowment Fund for Education (S-2648/LPDP.3/2014), the Medical Research Council  
551 (K501396) and the Wellcome Trust (106149).

552

## 553 **Author contributions**

554 DS, KA and AJ designed the study. DS collected the human data. WX and TMH collected the monkey  
555 data. DS, FG and AJ developed the computational model. DS and AJ wrote the manuscript with  
556 contributions from all other authors.

557

## 558 **Declaration of competing interests**

559 The authors declare no competing interests.

560

## 561 **Materials and Methods**

### 562 **Human experiments**

#### 563 Subjects

564 Based on pilot studies we decided in advance to use a sample size of eight subjects in each experiment.  
565 In total, we recruited 11 adult subjects in total at the Institute of Neuroscience, Newcastle University.  
566 Eight subjects (3 females; age 23–33; 1 left-handed) participated in both Experiment 1 (feedback  
567 delay) and Experiment 2 (feedback delay and spatial perturbation). Eight subjects (3 females; age 23–  
568 33; all right-handed) participated in Experiment 3 (feedforward task); 6 of these subjects also  
569 participated in experiments 1 and 2. Eight subjects (3 females; age 23–33; all right-handed)  
570 participated in the experiment shown in Figure S8; 7 out of these subjects also participated in  
571 Experiment 3. All experiments were approved by the local ethics committee at Newcastle University  
572 and performed after informed consent, which was given in accordance with the Declaration of  
573 Helsinki.

#### 574 Human tracking task

575 Subjects tracked a (red) target on a computer monitor by exerting bimanual isometric index finger  
576 forces on two sensors (FSG15N1A; Honeywell). The target underwent uniform, slow circular motion  
577 with a pseudorandom order of clockwise and anticlockwise directions across trials. Finger forces were  
578 sampled at 50 samples/s (USB-6343; National Instruments) and mapped to (yellow) cursor position by  
579 projecting onto two diagonal screen axis. In addition, a feedback delay ( $\tau_{\text{ext}}$ ) was interposed between  
580 force and cursor movement. The feedback delay was kept constant through the duration of each trial  
581 (lasting 20 s). We express screen coordinates in terms of the radius of target motion,  $r_{\text{target}} = 100\%$ .  
582 Tracking the target rotation thus required generating sinusoidal motion in the range of -100% to  
583 +100%, corresponding to finger forces of 0 to 3.26N, with a 90° phase-shift between each hand. At the  
584 end of each trial subjects were given a numerical score from 0-1000 indicating how accurately they  
585 tracked the target. Subjects were instructed to attempt to maximize this score, which was calculated  
586 as:

$$587 \quad \text{Score} = \frac{1000}{T} \times \int_0^T \left( 1 - e^{-\frac{|r_{\text{cursor}}(t) - r_{\text{target}}(t)|}{\delta}} \right) dt \quad (\text{Equ. 6})$$

588 where  $r_{\text{cursor}}(t)$  and  $r_{\text{target}}(t)$  are the 2D positions of the cursor and target respectively, and  $\delta =$   
589 50%. Apart from the experiment shown in Figure S8, all experiments used a frequency of target  
590 rotation,  $f_{\text{target}} = 0.2$  rotations per second.

591 Experiment 1 used five delay conditions ( $\tau_{\text{ext}} = 0, 100, 200, 300, \text{ or } 400$  ms). Subjects performed a  
592 total of 70 trials, comprising 14 of each condition presented in pseudorandom order.

593 For Experiment 2, spatial perturbations were added to the cursor position as well as time delays. The  
594 perturbations were equivalent to sinusoidal modulation of the target angular velocity, but were  
595 instead added to the cursor. Expressed in polar coordinates  $\mathbf{r} = \langle r, \angle \theta \rangle$  relative to the center of the  
596 screen, the target and cursor positions were thus given by:

$$597 \quad \mathbf{r}_{\text{target}}(t) = \langle r_{\text{target}}, \angle \omega_{\text{target}} t \rangle \quad (\text{Equ. 7})$$

$$598 \quad \mathbf{r}_{\text{pert}}(t) = \langle r_{\text{target}}, \angle \omega_{\text{target}} t + \frac{\omega_{\text{target}}}{\omega_{\text{pert}}} \sin \omega_{\text{pert}} t \rangle - \mathbf{r}_{\text{target}}(t) \quad (\text{Equ. 8})$$

$$599 \quad \mathbf{r}_{\text{cursor}}(t) = \langle r_{\text{force}}(t), \angle \theta_{\text{force}}(t) \rangle + \mathbf{r}_{\text{pert}}(t) \quad (\text{Equ. 9})$$

600 where  $\omega_{\text{target}} = 2\pi f_{\text{target}}$  is the angular velocity of the target around the centre of the screen,  
601  $\omega_{\text{pert}} = 2\pi f_{\text{pert}}$  is the angular frequency of the perturbation, and  $\langle r_{\text{force}}(t), \angle \theta_{\text{force}}(t) \rangle$  is the  
602 unperturbed cursor position calculated from the subject's forces at time  $t - \tau_{\text{ext}}$ .

603 Kinematic analyses were based on the time-varying angular velocity of the cursor subtended at the  
604 center of the screen:

$$605 \quad \omega_{\text{cursor}}(t) = \frac{d}{dt} \theta_{\text{cursor}}(t) \quad (\text{Equ. 10})$$

606 For spatial perturbation experiments, we also calculated the angular velocity of the unperturbed  
607 cursor position subtended at the center of the screen:

$$608 \quad \omega_{\text{force}}(t) = \frac{d}{dt} \theta_{\text{force}}(t) \quad (\text{Equ. 11})$$

609 Note that since  $r_{\text{force}} \approx r_{\text{target}}$ , the perturbation effectively adds a sinusoidal component to the  
610 angular velocity of the cursor:

$$611 \quad \omega_{\text{cursor}}(t) \approx \omega_{\text{force}}(t) + \omega_{\text{target}} \cos \omega_{\text{pert}} t \quad (\text{Equ. 12})$$

612 Six different spatial perturbations ( $f_{\text{pert}} = 0, 1, 2, 3, 4, 5$  Hz) combined with two feedback delays ( $\tau_{\text{ext}}$   
613 = 0, 200 ms) yielded 12 conditions. Subjects performed a total of 144 trials, comprising 12 trials per  
614 condition in pseudorandom order.

## 615 Human feedforward task

616 In Experiment 3, we used a unimanual isometric task in which subjects were asked to make sinusoidal  
617 forces with their right index finger. Subjects received visual feedback of the cursor, but no target was  
618 shown. Instead subjects were shown two amplitude boundaries to move between, and the frequency  
619 of movement was cued with auditory beeps at frequencies of 1, 2, 3, 4 and 5 Hz. Subjects performed  
620 a total of 15 trials, comprising three 20 s trials per frequency condition.

621

## 622 **Monkey experiments**

### 623 Subjects

624 We used two purpose-bred female rhesus macaques (monkey S: 6 years old, 6.6 kg; monkey U: 6 years  
625 old, 8.8 kg). Animal experiments were approved by the local Animal Welfare Ethical Review Board and  
626 performed under appropriate UK Home Office licenses in accordance with the Animals (Scientific  
627 Procedures) Act 1986.

### 628 Monkey tracking task



629 Monkeys moved a 2D computer cursor by generating isometric flexion-extension (vertical) and radial-  
630 ulnar (horizontal) torques at the wrist, measured by a 6-axis force/torque transducer (Nano25; ATI  
631 Industrial Automation). Centre-out targets were presented at 8 peripheral positions in a  
632 pseudorandom order. Targets were positioned at 70% of the distance to the screen edge (100%  
633 corresponding to torque of 0.67 Nm). The diameter of the target and cursor ranged between 14-36%.  
634 A successful trial required maintaining an overlap between cursor and peripheral target for 0.6 s after  
635 which the monkeys returned to the center of the screen to receive a food reward. Visual feedback of  
636 the cursor was delayed by  $\tau_{\text{ext}} = 0, 200, 400, 600$  ms throughout separate blocks of 50-70 trials each.  
637 Monkey S performed the task with the right hand. Monkey U initially used the right hand and was  
638 then retrained for a second period of data collection with the left hand.

### 639 LFP recording

640 LFPs were recorded using custom arrays of 12 moveable 50  $\mu\text{m}$  diameter tungsten microwires  
641 (impedance  $\sim 200$  k $\Omega$  at 1 kHz) chronically implanted in contralateral wrist area of M1 under  
642 sevoflurane anesthesia with postoperative analgesics and antibiotics. Head-free recordings were  
643 made using unity-gain headstages followed by wide-band amplification and sampling at 24.4  
644 kilosamples/s (System 3; Tucker-Davis Technologies). LFPs were digitally low-pass filtered at 200 Hz  
645 and recorded at 488 samples/second.

646 Analysis of kinematics and neural data was performed on data recorded over 8 different days  
647 comprising of 56 task blocks in Monkey S (no delay: 24 blocks; 200 ms delay: 13; 400 ms delay: 13; 600  
648 ms delay: 6), and 89 recording days comprising of 356 task blocks in Monkey U (no delay: 89; 200 ms  
649 delay: 89; 400 ms delay: 89; 600 ms delay: 89). Each task block comprised 50 (monkey S) or 70 trials  
650 (monkey U).

651

## 652 **Analysis Methods**

### 653 Human data analysis

654 Spectral analysis used fast Fourier transforms (FFTs) performed on non-overlapping 512 sample-point  
655 windows (approx. 10s) taken from the middle of each trial. Submovement peaks in the power spectra  
656 were measured after smoothing with a seven-point moving-average.

657 For perturbation experiments, we additionally defined two complex transfer functions  $H_{\text{cursor}}$  and  
658  $H_{\text{force}}$ :

$$659 \quad H_{\text{cursor}}(i\omega_{\text{pert}}) = \frac{2}{\omega_{\text{target}} T} \int_0^T \omega_{\text{cursor}}(t) e^{-i\omega_{\text{pert}} t} dt \quad (\text{Equ. 13})$$

$$660 \quad H_{\text{force}}(i\omega_{\text{pert}}) = \frac{2}{\omega_{\text{target}} T} \int_0^T \omega_{\text{force}}(t) e^{-i\omega_{\text{pert}} t} dt \quad (\text{Equ. 14})$$

661 Cursor and force amplitude responses to perturbations were calculated as the magnitude of the  
662 corresponding transfer functions, and the intrinsic phase delay of force responses was given by:

$$663 \quad \tau_{\varphi}(i\omega_{\text{pert}}) = -\frac{\arg[H_{\text{force}}(i\omega_{\text{pert}})]}{\omega_{\text{pert}}} - \tau_{\text{ext}} \quad (\text{Equ. 15})$$

664 Additionally, tracking performance was quantified off-line using the root-mean-squared Euclidean  
665 distance between cursor and target.

### 666 Monkey data analysis

667 We differentiated the magnitude of the absolute 2D torque (expressed as a percentage of the distance  
 668 to the edge of the screen) to obtain the radial cursor velocity. LFP channels were subjected to visual  
 669 inspection to reject noisy channels prior to mean-subtraction. For time-domain analysis, LFPs and  
 670 cursor velocities were low-pass filtered at 10 Hz. Submovements were defined as a peak radial cursor  
 671 speed exceeding 100%/s (monkey S) and 150%/s (monkey U). For frequency-domain analysis, we took  
 672 unfiltered sections of 1024 sample points from each trial (approx. 1.5 s before to 0.5 s after the end  
 673 of the peripheral hold period). We subtracted the trial-averaged profile from each section before  
 674 concatenating to yield long data sections without any consistent low-frequency components related  
 675 to the periodicity of the task. FFTs were calculated with overlapping Hanning windows ( $2^{14}$  sample  
 676 points  $\approx 34$  s; 75% overlap), from which we derived the following spectra:

677 Cursor power:  $P_{\text{Cursor}}(f) = \frac{\sum_{m=1}^M F_{\text{cursor}}(f,m) \cdot F_{\text{cursor}}(f,m)^*}{M}$

678 LFP power:  $P_{\text{LFP } i}(f) = \frac{\sum_{m=1}^M F_{\text{LFP } i}(f,m) \cdot F_{\text{LFP } i}(f,m)^*}{M}$

679 LFP-cursor coherence:  $\text{Coh}_{\text{LFP } i\text{-Cursor}} = \frac{|\sum_{m=1}^M F_{\text{LFP } i}(f,m) \cdot F_{\text{cursor}}(f,m)^*|^2}{M \cdot P_{\text{Cursor}}(f) \cdot P_{\text{LFP } i}(f)}$

680 LFP-LFP imaginary coherence:  $\text{Im Coh}_{\text{LFP } i\text{-LFP } j} = \frac{(\text{Im}[\sum_{m=1}^M F_{\text{LFP } i}(f,m) \cdot F_{\text{LFP } j}(f,m)^*])^2}{M \cdot P_{\text{LFP } i}(f) \cdot P_{\text{LFP } j}(f)}$

681 where  $F_{\text{LFP } i}(f, m)$  and  $F_{\text{Cursor}}(f, m)$  represent Fourier coefficients at frequency  $f$  and window  $m =$   
 682  $(1..M)$  from LFP channel  $i$  and cursor velocity respectively. All spectra were smoothed with a 16-point  
 683 Hanning window. In addition, LFP power and LFP-cursor coherence were averaged across all LFP  
 684 channels, while LFP-LFP imaginary coherence was averaged over all pairs of LFPs.

685

## 686 Modelling

687 Although both human and monkey tasks involved 2D isometric control, for simplicity we modelled  
 688 only a 1D controller and assumed a one-to-one mapping from control signal,  $u_k$  to position,  $x_k$ . We  
 689 neglected target motion and designed the controller to minimize the influence of stochastic motor  
 690 errors using delayed, noisy feedback of position. We set the model time step  $\Delta t = 0.01$  s, intrinsic  
 691 feedback delay  $\tau_{\text{int}} = 0.26$  s, and the ratio of process/measurement noise  $\rho = 250 \text{ s}^{-2}$  unless otherwise  
 692 stated. Steady-state Kalman gains were calculated using the function *kalman* in MATLAB, and the  
 693 resultant discrete time dynamic system (Equ. 4) was implemented by two integrating neuronal  
 694 populations representing  $\hat{x}_k$  and  $\hat{v}_k$ , receiving a synaptic input on each time-step equal to:

695 
$$\begin{bmatrix} \Delta \hat{x}_k \\ \Delta \hat{v}_k \end{bmatrix} = \begin{bmatrix} -K_{\text{pos}} & \Delta t \\ -K_{\text{vel}} & 0 \end{bmatrix} \begin{bmatrix} \hat{x}_{k-1} \\ \hat{v}_{k-1} \end{bmatrix} + \begin{bmatrix} K_{\text{pos}} \\ K_{\text{vel}} \end{bmatrix} y_k \quad (\text{Equ. 16})$$

696 Two LFP components were simulated by normalizing  $\Delta \hat{x}_k$  and  $\Delta \hat{v}_k$  to unity variance, before adding  
 697 background common noise with a  $1/f$  spectrum.

698 The motor command  $u_k$  was generated on each time step using the Smith Predictor architecture  
 699 shown in Fig. 3F. Based on our observation that trajectory variability was maximal at times when force  
 700 output was changing (Figure S8), we used an linear quadratic regulator (LQR) control framework to  
 701 minimize a quadratic cost function,  $J$ , incorporating the rate of change in motor command,  $\frac{\Delta u_k}{\Delta t}$ :

702 
$$J = \sum_k \left( q x_k^2 + r \left( \frac{\Delta u_k}{\Delta t} \right)^2 \right) \quad (\text{Equ. 17})$$

703 For a state transition matrix in the form:

$$704 \begin{bmatrix} x_k \\ v_k \end{bmatrix} = \begin{bmatrix} 1 & \Delta t \\ 0 & 1 \end{bmatrix} \begin{bmatrix} x_{k-1} \\ v_{k-1} \end{bmatrix} + \begin{bmatrix} 0 \\ 1 \end{bmatrix} \frac{\Delta u_k}{\Delta t} \quad (\text{Equ. 18})$$

705  $J$  is minimized by a state feedback policy of the form:

$$706 \frac{\Delta u_k}{\Delta t} = - \begin{bmatrix} K_I \\ K_P \end{bmatrix} \cdot \begin{bmatrix} x_k \\ v_k \end{bmatrix} \quad (\text{Equ. 19})$$

707 which can be integrated to yield a PI controller:

$$\begin{aligned} 708 \quad u_k &= \sum_{j=1}^k \Delta u_j \\ 709 \quad &= -K_P \sum_{j=1}^k v_j \Delta t - K_I \sum_{j=1}^k x_j \Delta t \\ 710 \quad &= -K_P x_k - K_I \sum_{j=1}^k x_j \Delta t \end{aligned} \quad (\text{Equ. 20})$$

711 We found the proportional and integral gains  $K_P$  and  $K_I$  using the function *lqr* in MATLAB with  $q = 1$   
712 and  $r = \Delta t^2$ . In the full model, this controller acted on the optimal estimate of position,  $\hat{z}_k$ , after  
713 incorporating the delay feedback loop of the Smith Predictor. Note that the transfer function of a PI  
714 controller inside the fast feedback loop of the Smith Predictor is given by (Abe and Yamana, 2003):

$$715 H_{PI}(i\omega) = \frac{K_P + K_I/i\omega}{1 + K_P + K_I/i\omega} \quad (\text{Equ. 21})$$

716 which equals 1 for  $\omega = 0$  but tends to  $\frac{K_P}{1+K_P}$  at higher frequencies. Therefore this effectively reduces  
717 the response amplitude to perturbations. The full transfer function of the intrinsic dynamics, including  
718 time-delay is given by:

$$719 H_{\text{force}}(i\omega) = e^{-i\omega(\tau_{\text{int}} + \tau_{\text{ext}})} H_{PI}(i\omega) \cdot H_{y \rightarrow \hat{z}}(i\omega) \quad (\text{Equ. 22})$$

$$720 H_{\text{cursor}}(i\omega) = 1 - H_{\text{force}}(i\omega) \quad (\text{Equ. 23})$$

721 where  $H_{y \rightarrow \hat{z}}(i\omega)$  is the transfer function of the Kalman filter relating delayed position measurement  
722 to optimal position estimate.

723

## 724 **Data and software availability**

725 Datasets from the human and monkey experiments, sample analysis code and modelling associated  
726 with this work are available on Dryad doi:10.5061/dryad.53sq7kn.

## 727 References

- 728 Abe, N. and Yamanaka, K. (2003) 'Smith predictor control and internal model control - a tutorial',  
729 *SICE 2003 Annual Conference*, 2, pp. 1383-1387.
- 730 Amzica, F. and Steriade, M. (1997) 'The K-complex: its slow (<1-Hz) rhythmicity and relation to delta  
731 waves', *Neurology*, 49(4), pp. 952-9.
- 732 Churchland, M.M., Cunningham, J.P., Kaufman, M.T., Foster, J.D., Nuyujukian, P., Ryu, S.I. and  
733 Shenoy, K.V. (2012) 'Neural population dynamics during reaching', *Nature*, 487(7405), pp. 51-6.
- 734 Churchland, M.M., Cunningham, J.P., Kaufman, M.T., Ryu, S.I. and Shenoy, K.V. (2010) 'Cortical  
735 preparatory activity: representation of movement or first cog in a dynamical machine?', *Neuron*,  
736 68(3), pp. 387-400.
- 737 Craik, K.J. (1947) 'Theory of the human operator in control systems; the operator as an engineering  
738 system', *Br J Psychol Gen Sect*, 38(Pt 2), pp. 56-61.
- 739 Doeringer, J.A. and Hogan, N. (1998) 'Intermittency in preplanned elbow movements persists in the  
740 absence of visual feedback', *J Neurophysiol*, 80(4), pp. 1787-99.
- 741 Gawthrop, P., Loram, I., Lakie, M. and Gollee, H. (2011) 'Intermittent control: a computational theory  
742 of human control', *Biol Cybern*, 104(1-2), pp. 31-51.
- 743 Hall, T.M., de Carvalho, F. and Jackson, A. (2014) 'A common structure underlies low-frequency  
744 cortical dynamics in movement, sleep, and sedation', *Neuron*, 83(5), pp. 1185-99.
- 745 Hogan, N. and Sternad, D. (2012) 'Dynamic primitives of motor behavior', *Biol Cybern*, 106(11-12),  
746 pp. 727-39.
- 747 Jerbi, K., Lachaux, J.P., N'Diaye, K., Pantazis, D., Leahy, R.M., Garnero, L. and Baillet, S. (2007)  
748 'Coherent neural representation of hand speed in humans revealed by MEG imaging', *Proc Natl Acad  
749 Sci U S A*, 104(18), pp. 7676-81.
- 750 Jones, K.E., Hamilton, A.F. and Wolpert, D.M. (2002) 'Sources of signal-dependent noise during  
751 isometric force production', *J Neurophysiol*, 88(3), pp. 1533-44.
- 752 Kleinman, D.L. (1974) 'Towards Modeling Human Information Processing and Control in Economic  
753 Systems: An Approach Based On Manned Vehicle Systems Analysis', *Annals of Economic and Social  
754 Measurement*, 3(1), pp. 117-134.
- 755 Koken, P.W. and Erkelens, C.J. (1992) 'Influences of hand movements on eye movements in tracking  
756 tasks in man', *Exp Brain Res*, 88(3), pp. 657-64.
- 757 Kunesch, E., Binkofski, F. and Freund, H.J. (1989) 'Invariant temporal characteristics of manipulative  
758 hand movements', *Exp Brain Res*, 78(3), pp. 539-46.
- 759 Kwon, O.S., Tadin, D. and Knill, D.C. (2015) 'Unifying account of visual motion and position  
760 perception', *Proc Natl Acad Sci U S A*, 112(26), pp. 8142-7.
- 761 Loram, I.D., Gawthrop, P.J. and Lakie, M. (2006) 'The frequency of human, manual adjustments in  
762 balancing an inverted pendulum is constrained by intrinsic physiological factors', *J Physiol*, 577(Pt 1),  
763 pp. 417-32.
- 764 Miall, R.C. (1996) 'Task-dependent changes in visual feedback control: a frequency analysis of human  
765 manual tracking', *J Mot Behav*, 28(2), pp. 125-35.
- 766 Miall, R.C., Weir, D.J. and Stein, J.F. (1993a) 'Intermittency in human manual tracking tasks', *J Mot  
767 Behav*, 25(1), pp. 53-63.
- 768 Miall, R.C., Weir, D.J., Wolpert, D.M. and Stein, J.F. (1993b) 'Is the cerebellum a smith predictor?', *J  
769 Mot Behav*, 25(3), pp. 203-16.
- 770 Mulliken, G.H., Musallam, S. and Andersen, R.A. (2008) 'Forward estimation of movement state in  
771 posterior parietal cortex', *Proc Natl Acad Sci U S A*, 105(24), pp. 8170-7.
- 772 Pereira, M., Sobolewski, A. and Millan, J.D.R. (2017) 'Action Monitoring Cortical Activity Coupled to  
773 Submovements', *eNeuro*, 4(5), pp. 0241-17.
- 774 Russell, D.M. and Sternad, D. (2001) 'Sinusoidal visuomotor tracking: intermittent servo-control or  
775 coupled oscillations?', *J Mot Behav*, 33(4), pp. 329-49.
- 776 Russo, A.A., Bittner, S.R., Perkins, S.M., Seely, J.S., London, B.M., Lara, A.H., Miri, A., Marshall, N.J.,  
777 Kohn, A., Jessell, T.M., Abbott, L.F., Cunningham, J.P. and Churchland, M.M. (2018) 'Motor Cortex

778 Embeds Muscle-like Commands in an Untangled Population Response', *Neuron*, 97(4), pp. 953-  
779 966.e8.  
780 Scott, S.H. (2004) 'Optimal feedback control and the neural basis of volitional motor control', *Nat*  
781 *Rev Neurosci*, 5(7), pp. 532-46.  
782 Streng, M.L., Popa, L.S. and Ebner, T.J. (2018) 'Modulation of sensory prediction error in Purkinje  
783 cells during visual feedback manipulations', *Nat Commun*, 9(1), p. 1099.  
784 Todorov, E. and Jordan, M.I. (2002) 'Optimal feedback control as a theory of motor coordination',  
785 *Nat Neurosci*, 5(11), pp. 1226-35.  
786 Vince, M.A. (1948) 'The intermittency of control movements and the psychological refractory  
787 period', *Br J Psychol Gen Sect*, 38(Pt 3), pp. 149-57.  
788 Viviani, P. and Flash, T. (1995) 'Minimum-jerk, two-thirds power law, and isochrony: converging  
789 approaches to movement planning', *J Exp Psychol Hum Percept Perform*, 21(1), pp. 32-53.  
790 Woodworth, R.S. (1899) 'Accuracy of voluntary movement.', *The Psychological Review: Monograph*  
791 *Supplements*, 3(3), p. 114.  
792



793 **Supplemental Information**

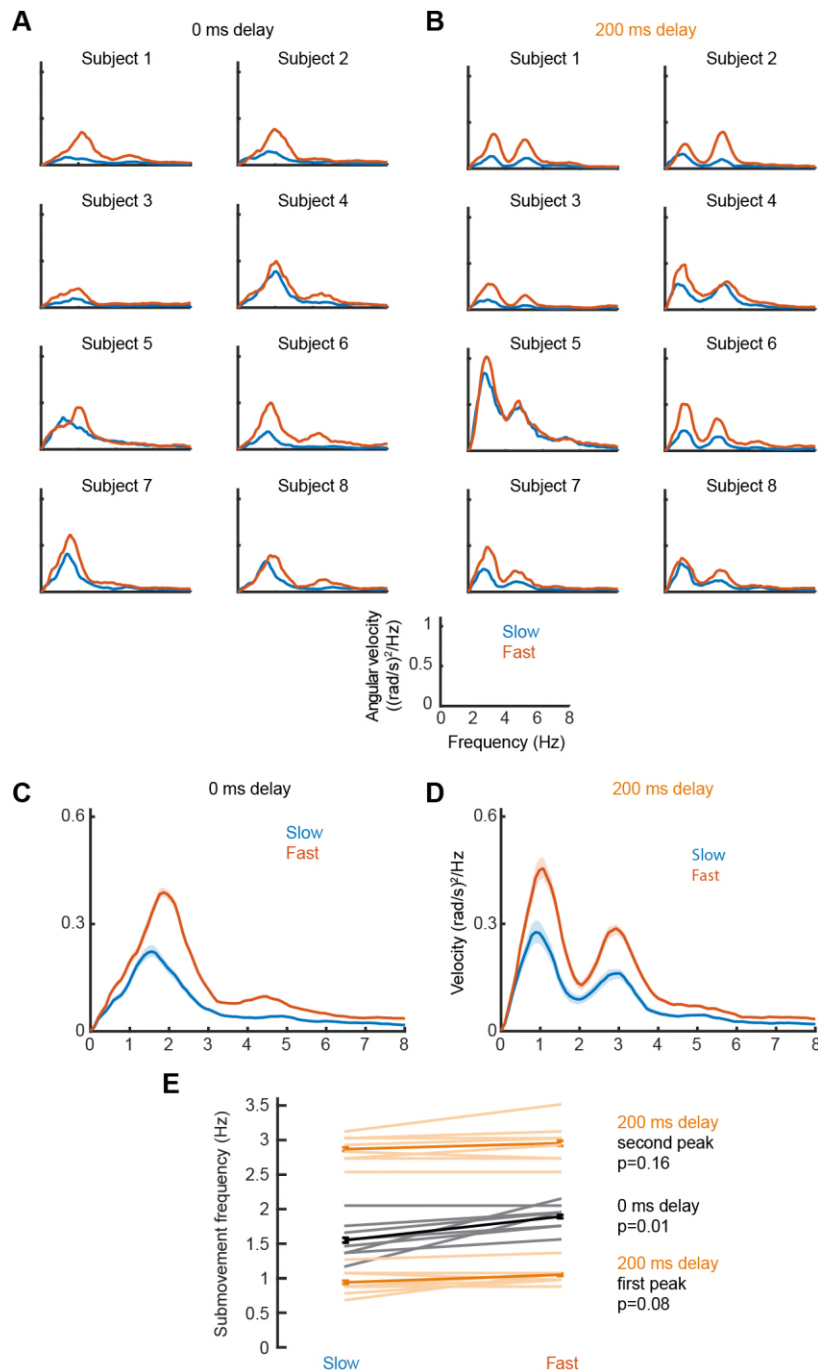
794

795 **Table S1. The dependency of submovement period on feedback delay.** Shown in the table are the  
 796 gradients and intercepts of regression lines fitted to each harmonic group in Figure 1E. The time period of each  
 797 spectral peak was regressed against feedback delay. Shown in square brackets are 95% confidence intervals of  
 798 these values. Also shown is the estimated intrinsic time delay calculated using Equ. 1.

799

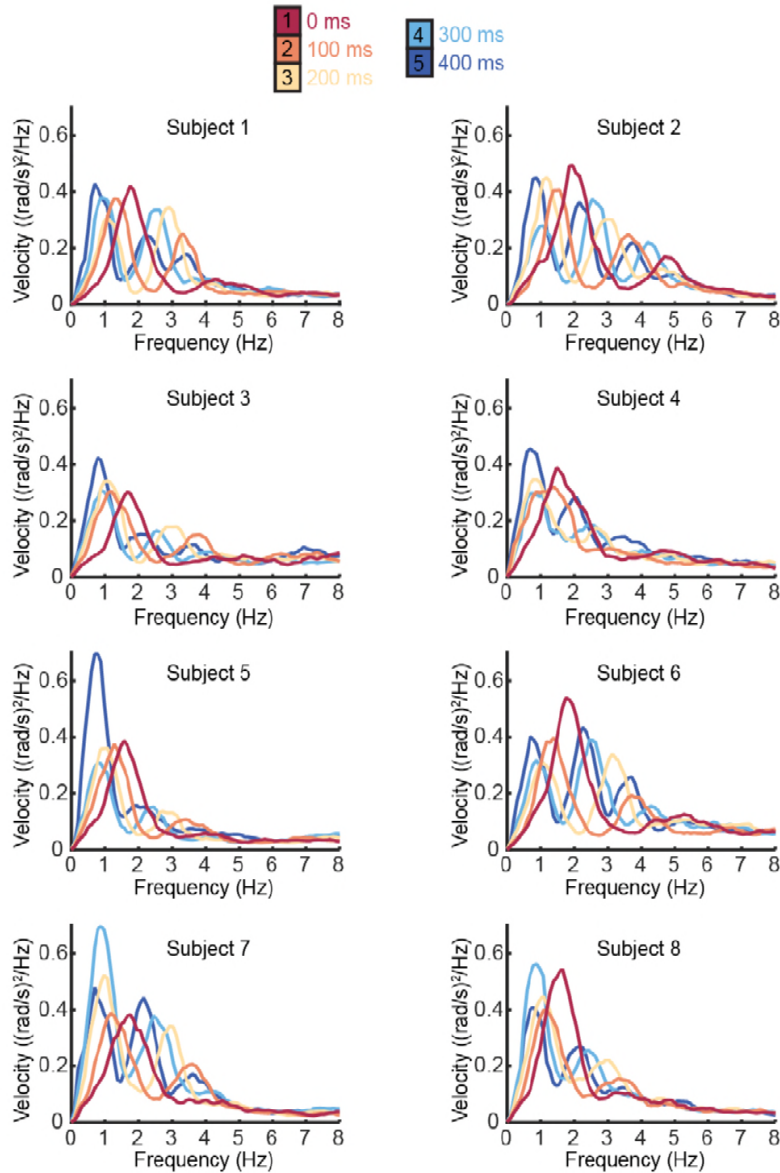
Harmonic ( <i>N</i> )	Predicted slope = $2/N$	Measured slope	Measured intercept (ms)	$R^2$	$P$	$\tau_{\text{int}} = \text{Intercept} * N/2$
1	2	1.89 [1.69,2.09]	589 ms [539,638]	0.90	<0.00001	294 ms [270,319]
3	0.67	0.59 [0.53,0.65]	226 ms [211,242]	0.94	<0.00001	340 ms [316,362]
5	0.4	0.33 [0.22,0.45]	146 ms [106,185]	0.75	<0.00001	364 ms [266,463]

800



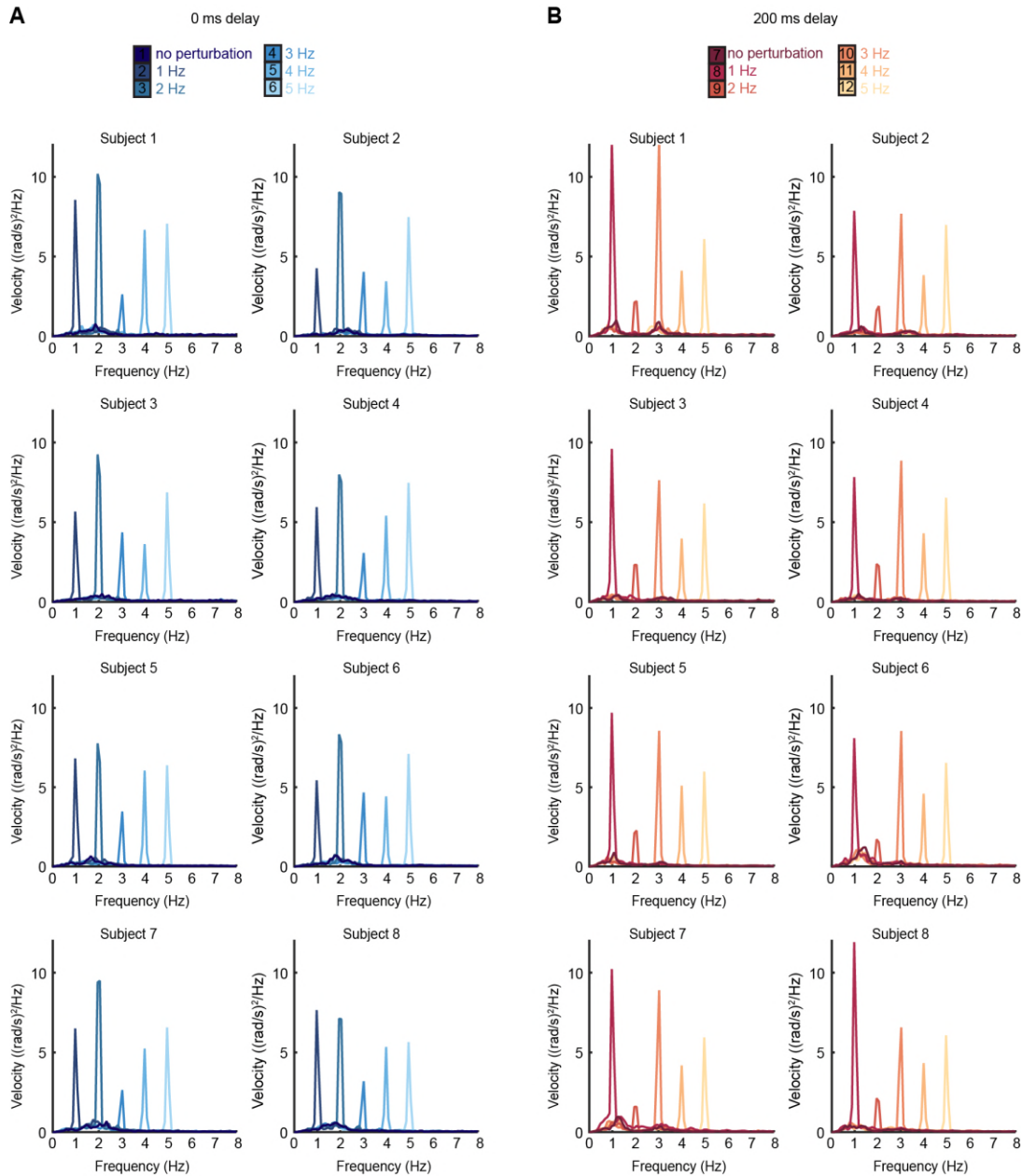
801

802 **Figure S1. Effect of target speed on movement intermittency.** (A) Power spectra of cursor angular  
 803 velocity for individual subjects with slow (0.1 cycles/s) or fast (0.2 cycles/s) target rotation, and no  
 804 feedback delay. (B) Power spectra of cursor angular velocity with slow or fast target rotation, and 200  
 805 ms feedback delay. (C,D) Average power, showing mean  $\pm$  s.e.m. for 8 subjects. (E) Average  $\pm$  s.e.m.  
 806 frequencies of peak cursor velocity in each condition. P values calculated using a paired t-test.



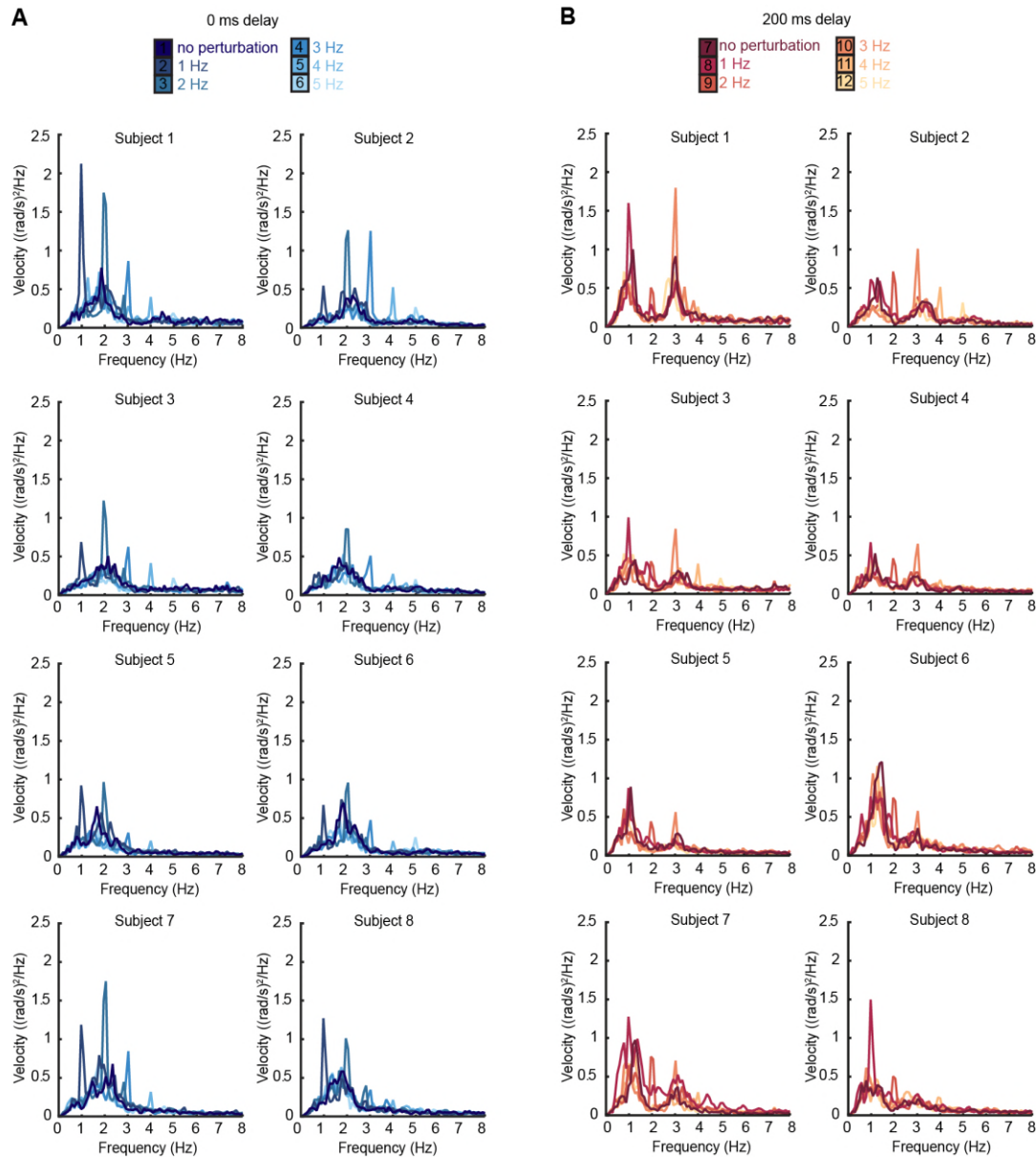
807

808 **Figure S2. Individual subject power spectra of cursor velocity with different feedback delays.** Power  
809 spectra of cursor angular velocity for individual subjects with 0–400 ms feedback delay. The average  
810 over subjects is shown in Figure 1D.



811

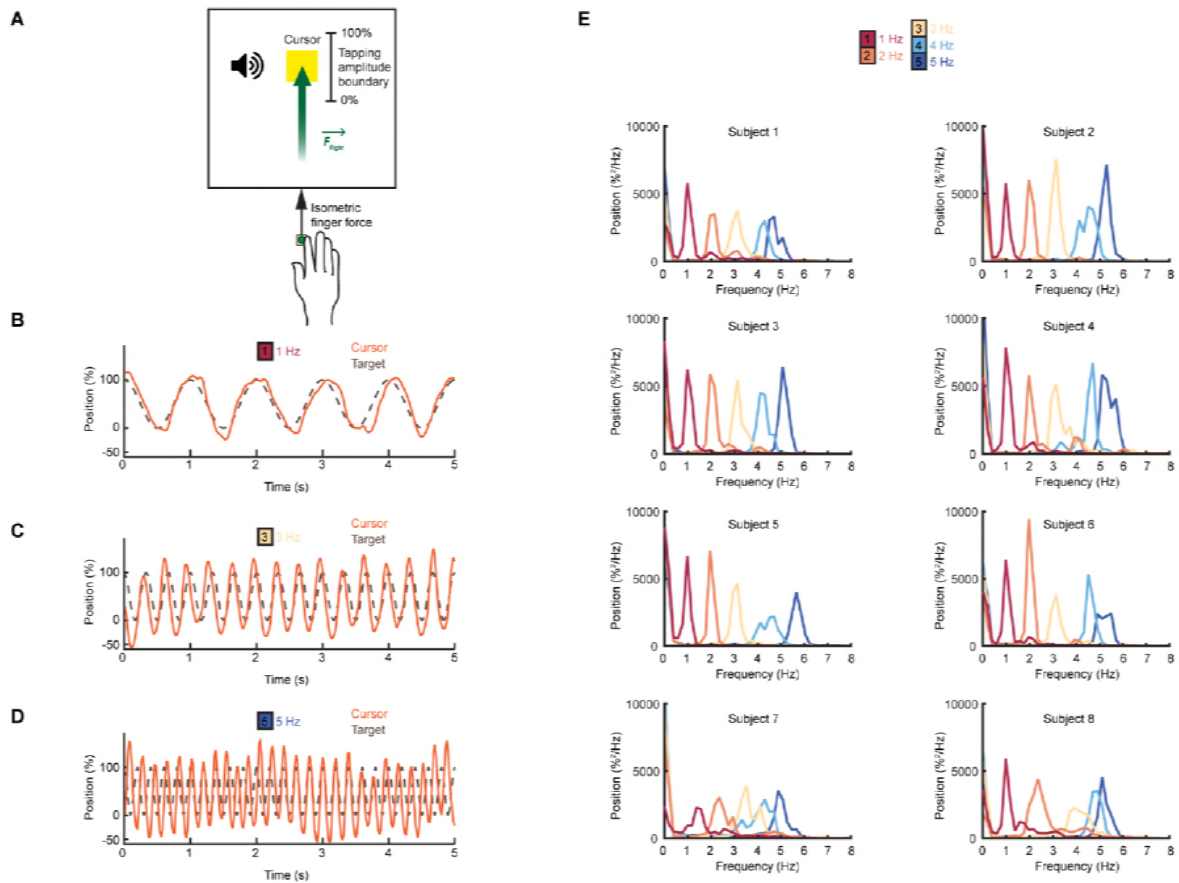
812 **Figure S3. Individual subject power spectra of cursor velocity with perturbations.** (A) Power spectra  
813 of cursor angular velocity for individual subjects with 1–5 Hz perturbations and no feedback delay. The  
814 average over subjects is shown in Figure 2C. (B) Power spectra of cursor angular velocity for individual  
815 subjects with 1–5 Hz perturbations and 200 ms feedback delay. The average over subjects is shown in  
816 Figure 2D.



817

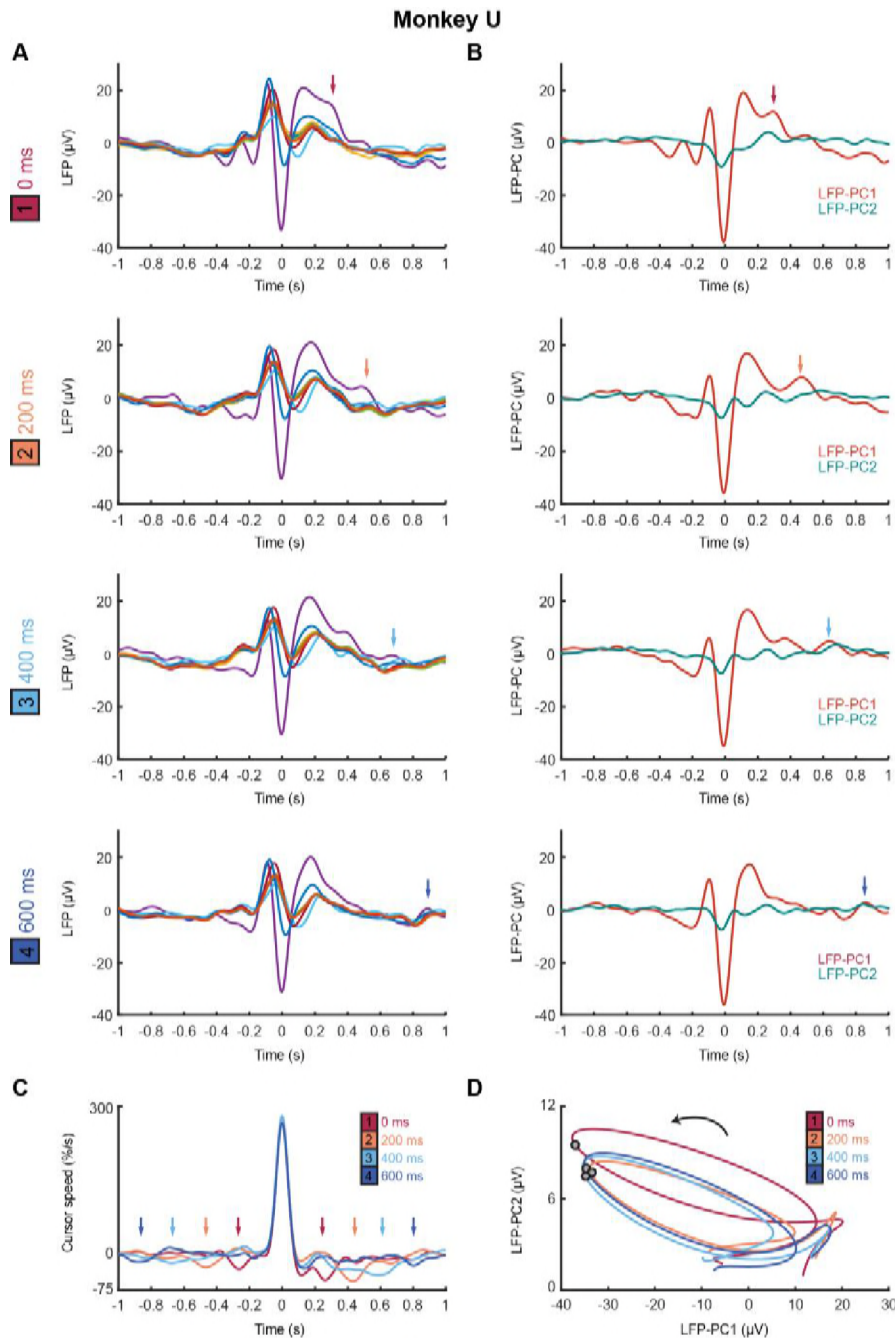
818 **Figure S4. Individual subject power spectra of force velocity with perturbations.** (A) Power spectra  
819 of force angular velocity for individual subjects with 1–5 Hz perturbations and no feedback delay. The  
820 average over subjects is shown in Figure 2F. (B) Power spectra of force angular velocity for individual  
821 subjects with 1–5 Hz perturbations and 200 ms feedback delay. The average over subjects is shown in  
822 Figure 2G.





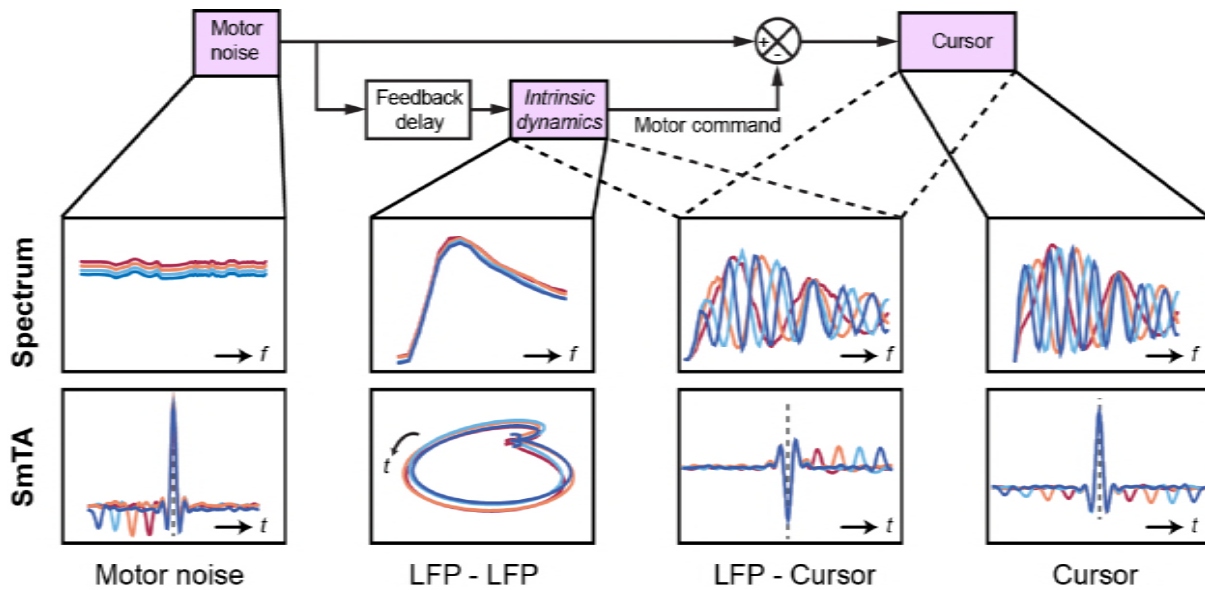
823

824 **Figure S5. Feedforward task.** (A) Schematic of the feedforward isometric task. Subjects generated  
825 sinusoidal forces within a set range, at a frequency indicated by an auditory cue. (B-D) Performance  
826 of an example subject for frequencies between 1-5 Hz. (E) Power spectrum of force for individual  
827 subjects. The average over all subjects is shown in Figure 2J.



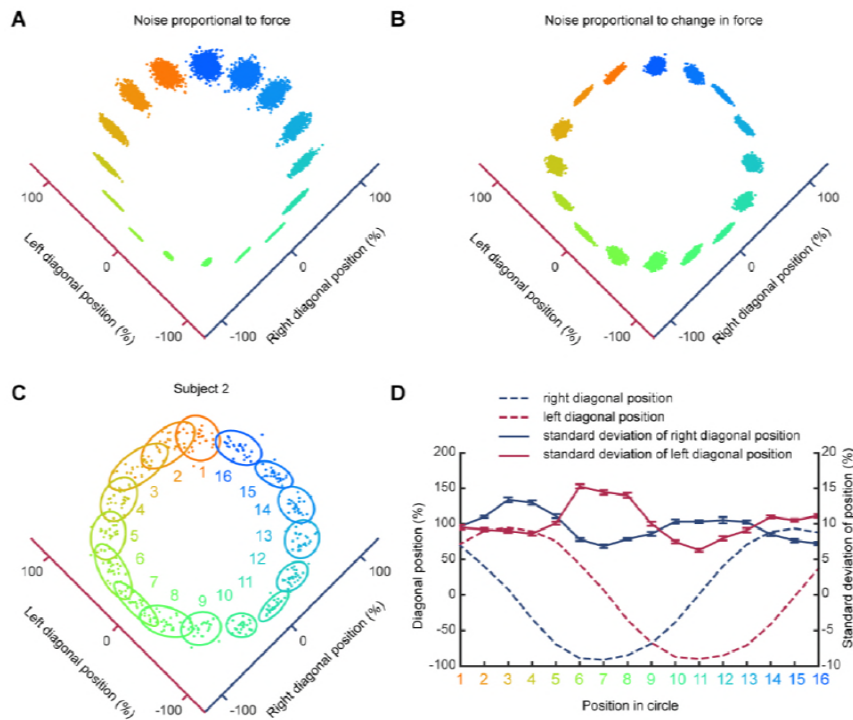
828

829 **Figure S6. Submovement-triggered averages of M1 LFPs for Monkey U.** (A) Average low-pass filtered  
830 LFPs from M1, aligned to the peak speed of submovements with 0–600 ms feedback delay. Arrows  
831 indicate second feature following submovement by an extrinsic delay-dependent latency. Data from  
832 Monkey U. (B) Average of first two LFP-PCs aligned to submovements. (C) Average low-pass filtered  
833 cursor speed, aligned to submovements. Arrows indicate symmetrical velocity troughs at extrinsic  
834 delay-dependent latencies. (D) Average submovement-triggered LFP-PC trajectories, plotted over 200  
835 ms either side of the time of peak submovement speed (indicated by circles).



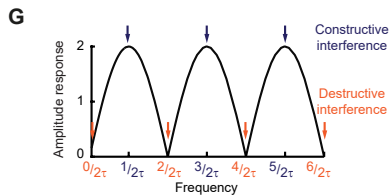
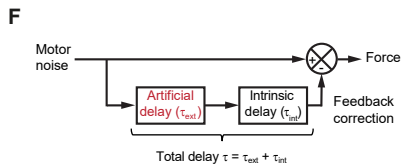
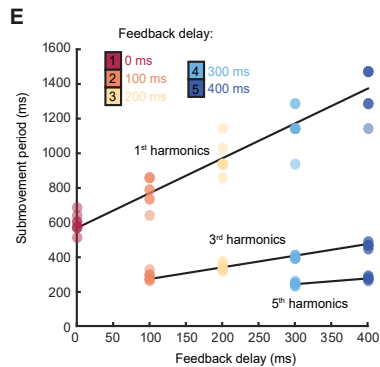
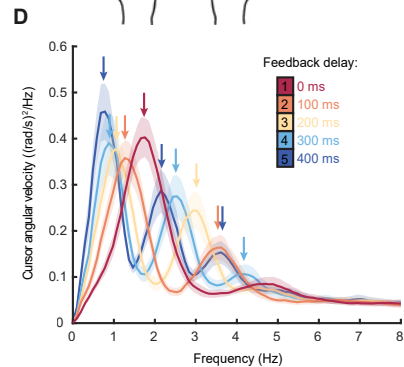
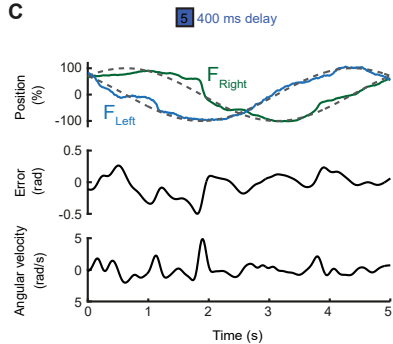
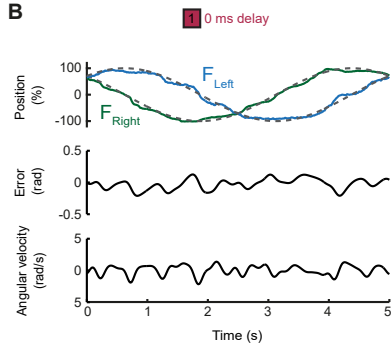
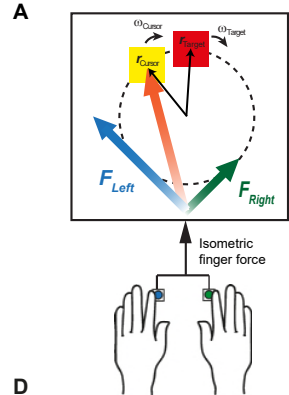
836

837 **Figure S7. Schematic of delay-dependent and delay-independent relationships in OFC model.** The  
 838 boxes show how the various frequency-domain and submovement-triggered average (SmTA)  
 839 relationships are explained by the OFC model. *Top row*, from left to right: Broad spectrum motor noise  
 840 drives intrinsic dynamics resulting in a delay-independent LFP cross-spectral resonance. The delayed  
 841 motor command is combined with the original motor noise leading to delay-dependent comb filtering  
 842 evident in LFP-Cursor coherence and Cursor power spectrum. *Bottom row*, from left to right:  
 843 submovements can arise from a positive noise peak at time-zero, or as a correction to a preceding  
 844 negative noise trough. Due to intrinsic dynamics, LFPs trace consistent cyclical trajectories locked to  
 845 submovements. SmTA of LFPs contains potentials associated with noise peak/troughs after feedback  
 846 delay. SmTA of cursor velocity combines noise with delayed feedback corrections to yield a central  
 847 submovement flanked by symmetrical troughs.

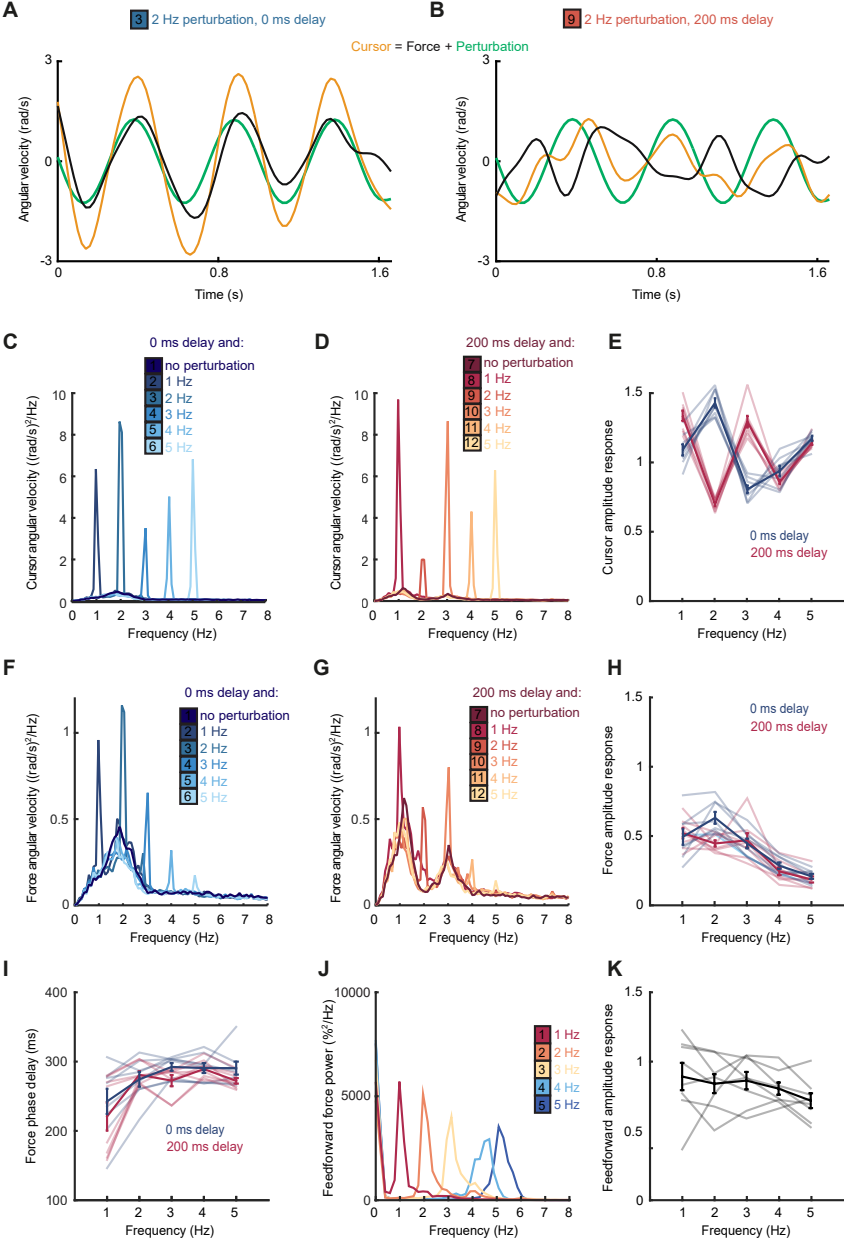


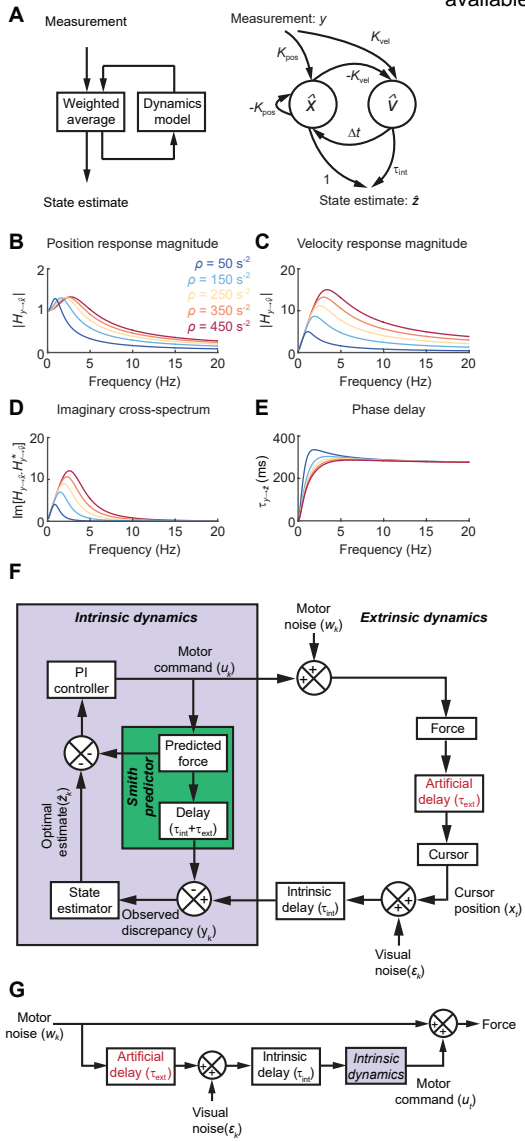
848

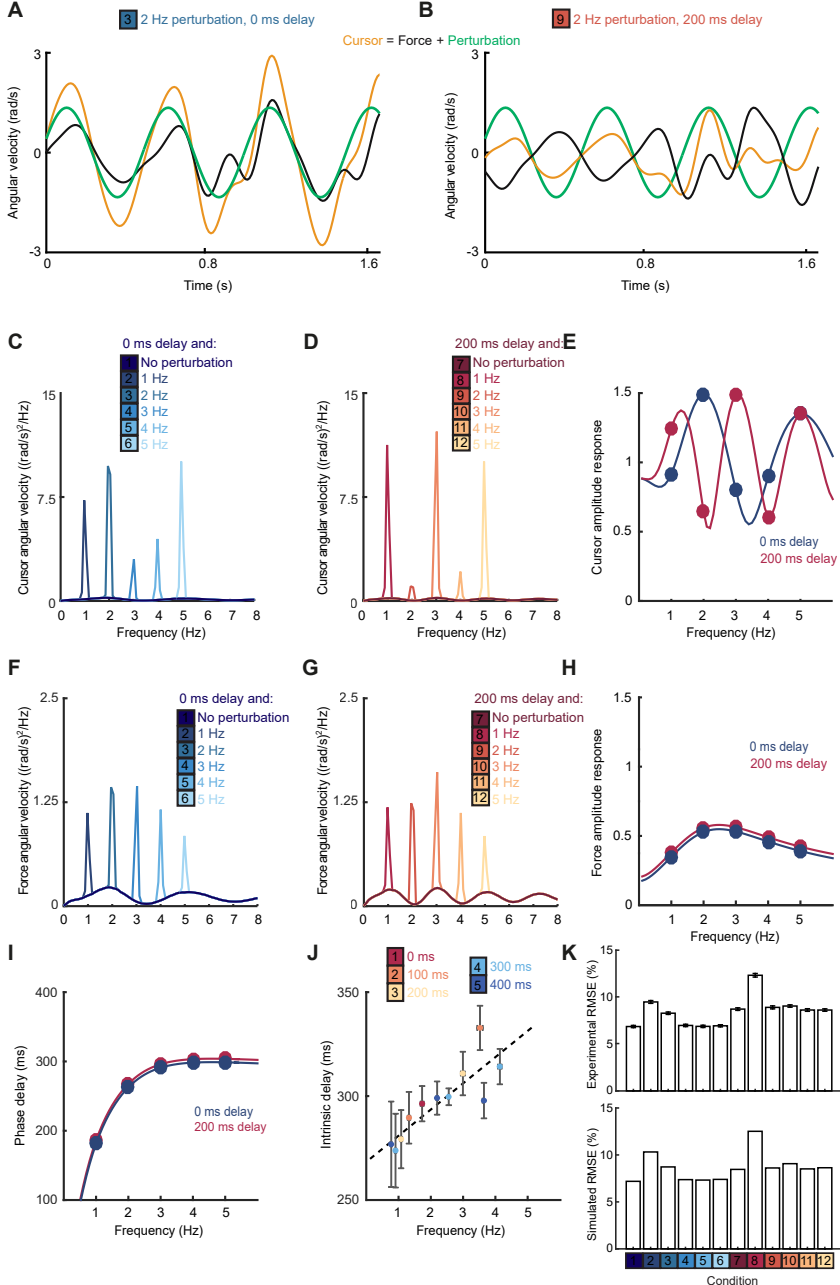
849 **Figure S8. Trajectory variability depends on change in isometric force.** (A) Simulated pattern of trial-  
850 to-trial variability if motor noise is proportional to absolute force. (B) Simulated pattern of trial-to-trial  
851 variability if motor noise is proportional to derivative of force. (C) Variability of a typical subject during  
852 counter clockwise tracking. 2D cursor position over multiple trials and associated covariance ellipses  
853 are shown for 16 target positions. (D) Average and s.e.m. of standard deviation of force along each  
854 finger axis for the 16 target positions. Note that variability is maximal at times of maximal change in  
855 associated finger force (*dashed lines*).

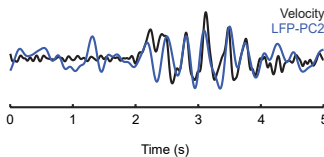
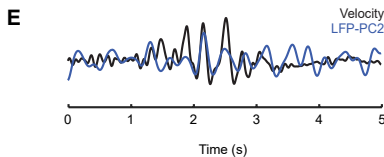
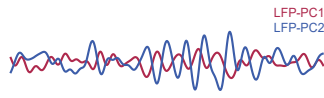
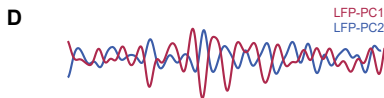
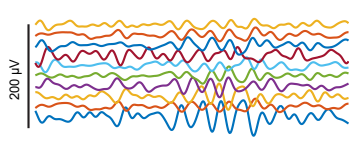
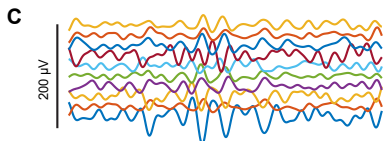
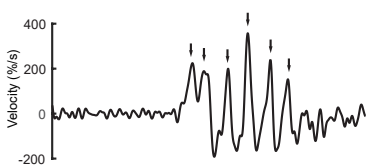
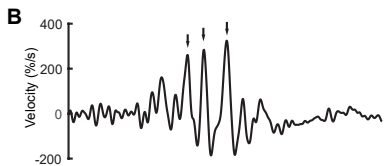
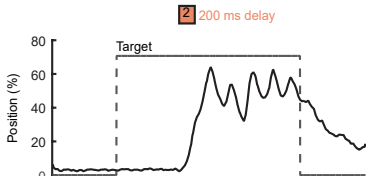
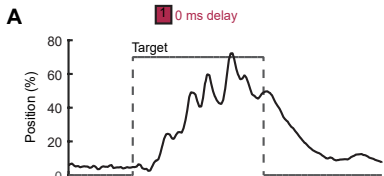


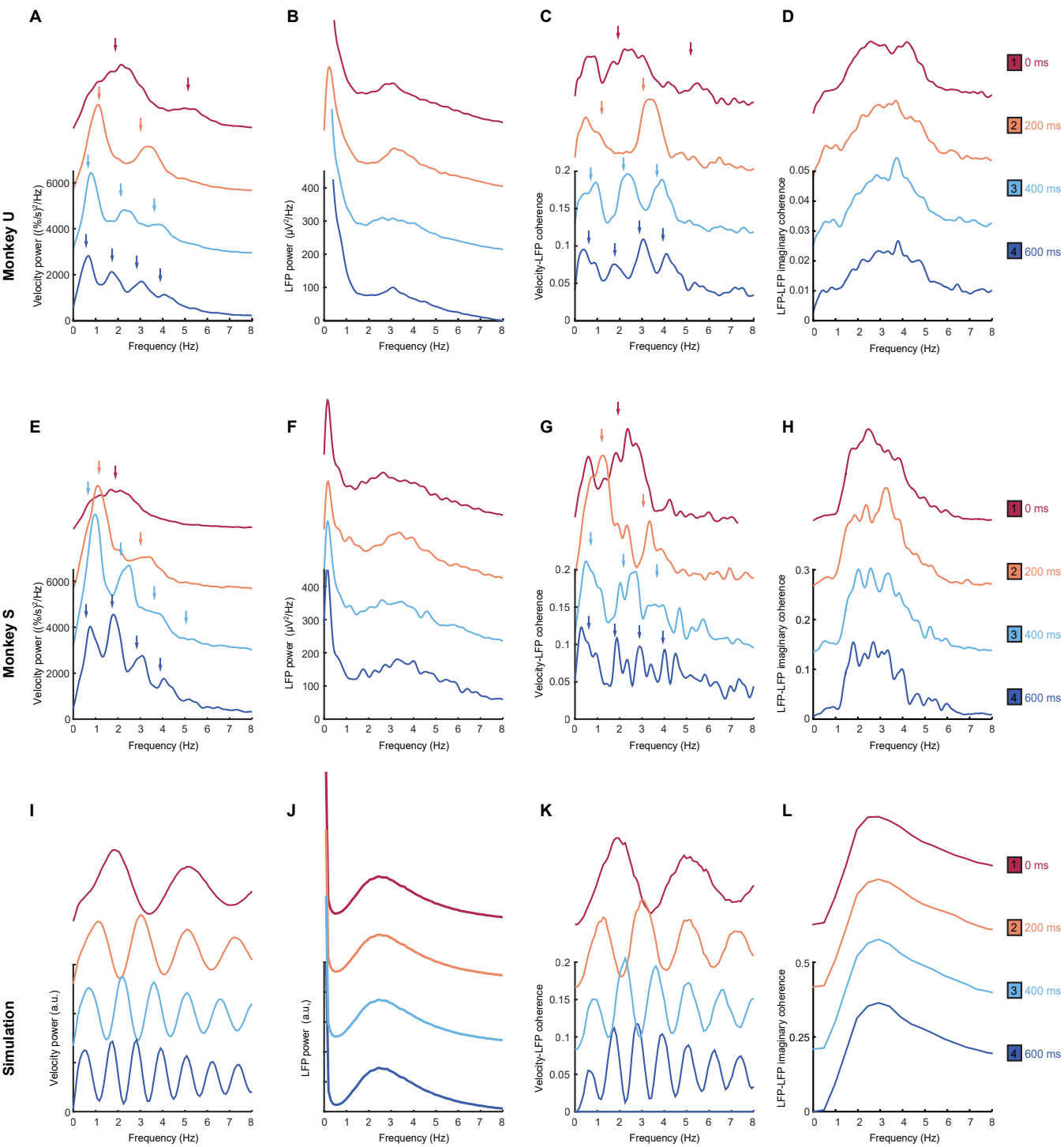




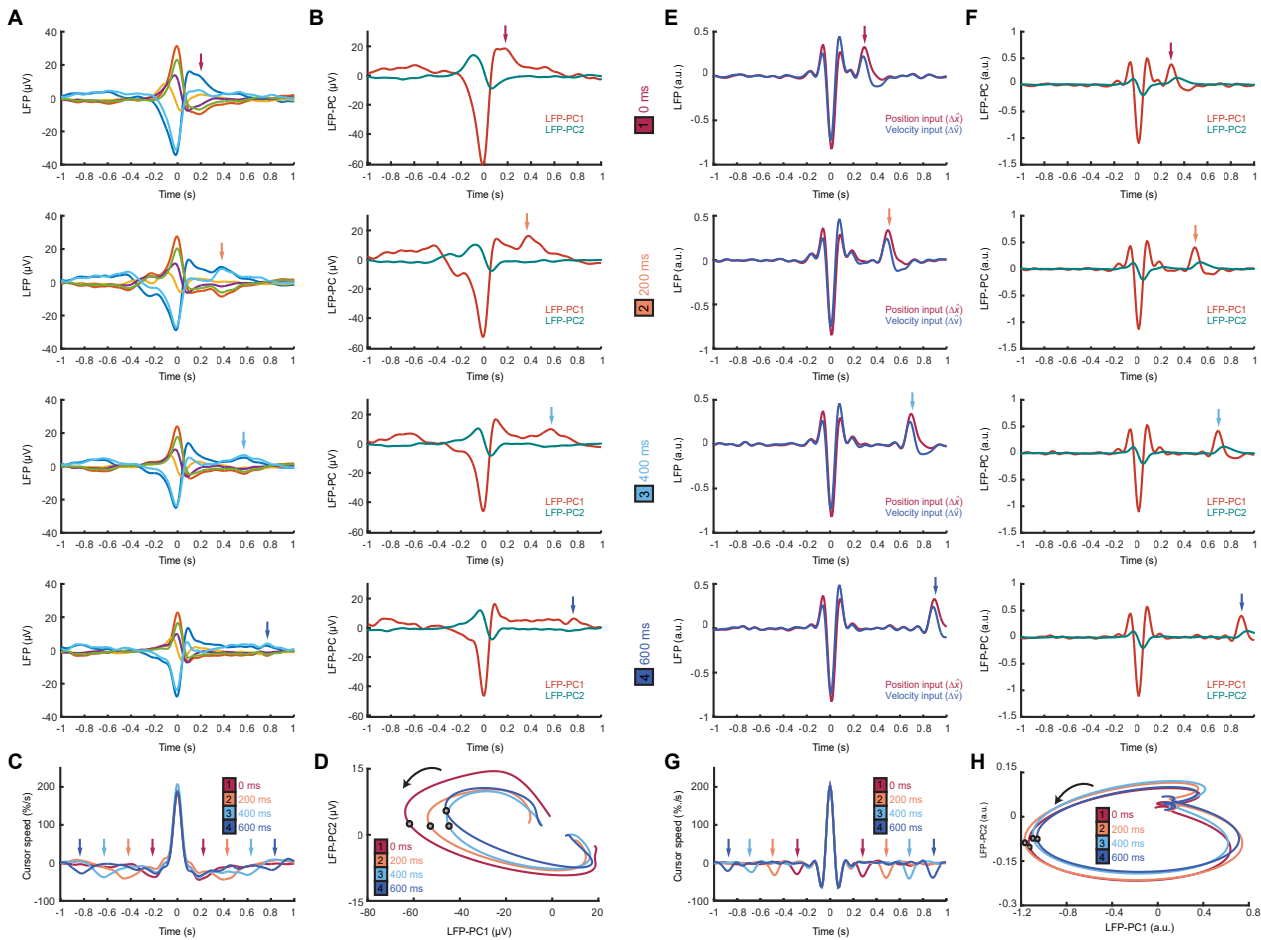






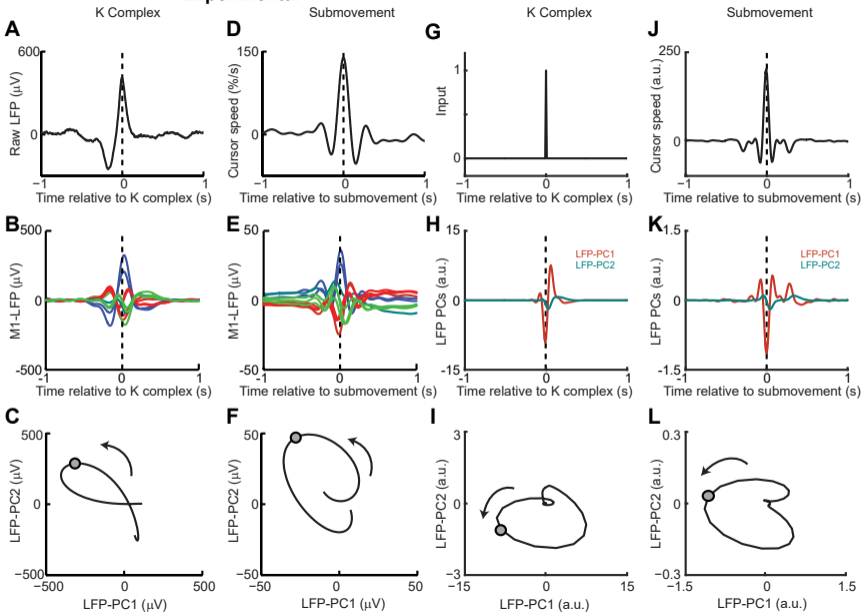


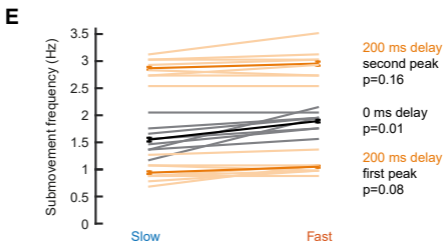
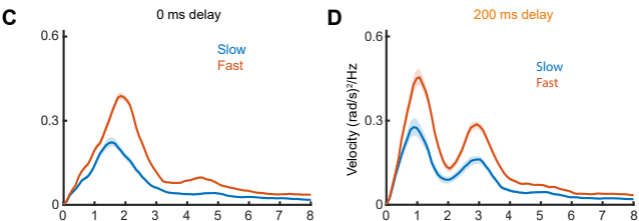
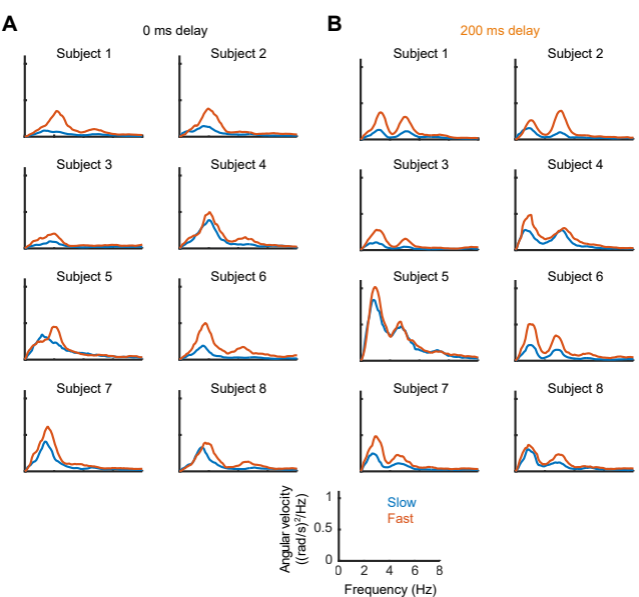




## Experimental

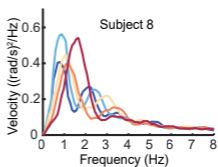
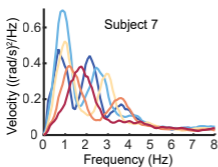
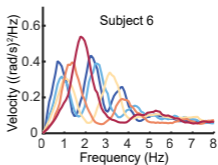
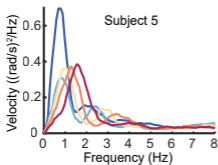
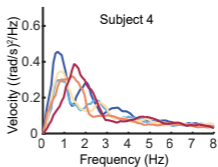
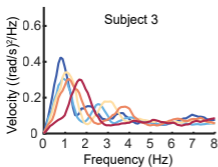
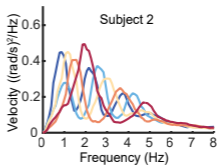
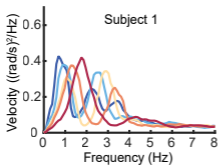
## Simulation





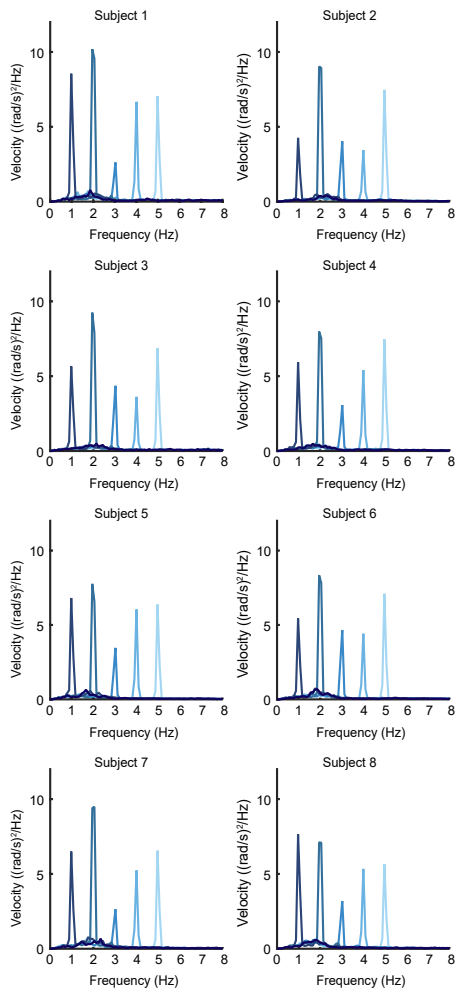
1 0 ms  
2 100 ms  
3 200 ms

4 300 ms  
6 400 ms

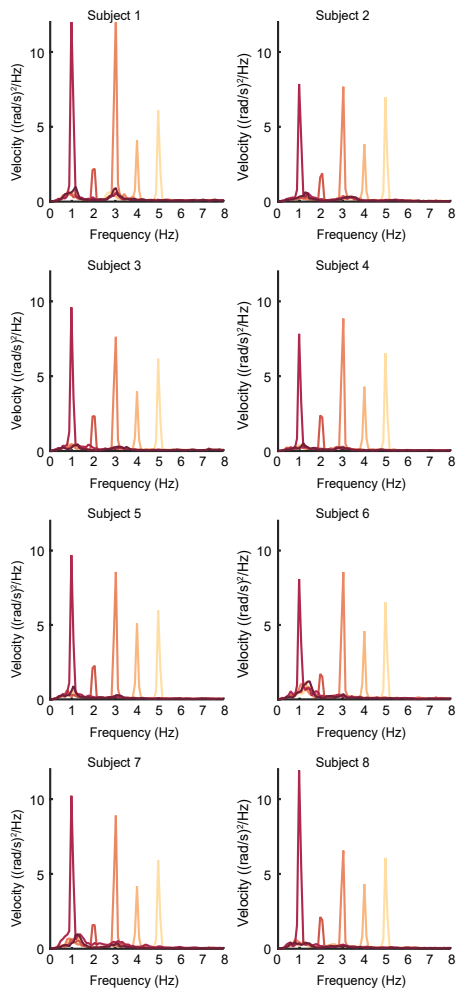
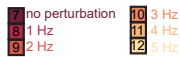


**A**

0 ms delay

**B**

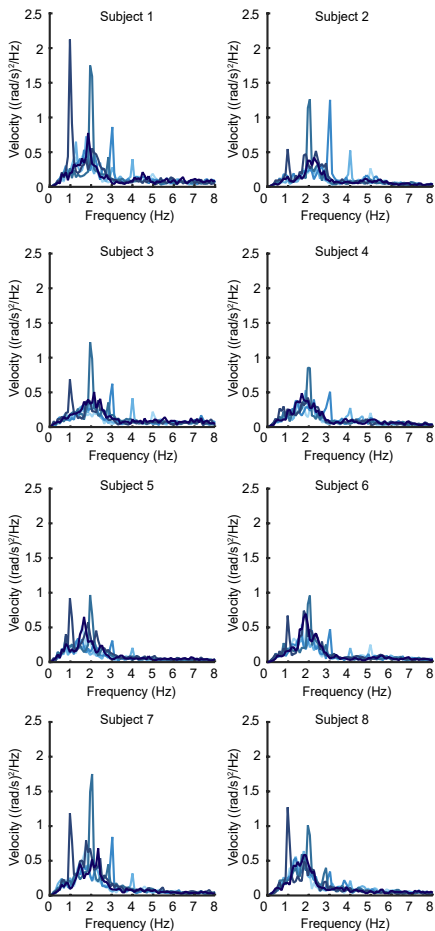
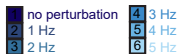
200 ms delay



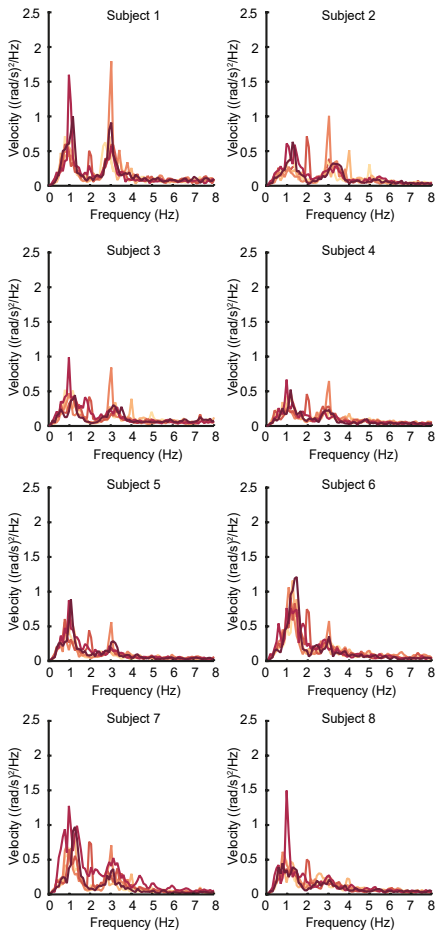
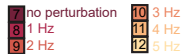


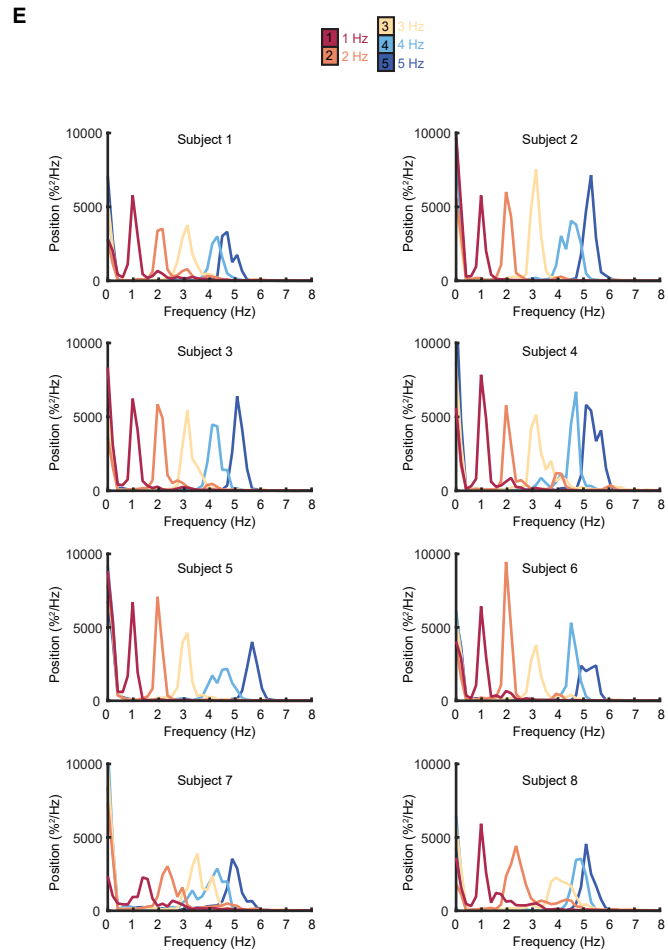
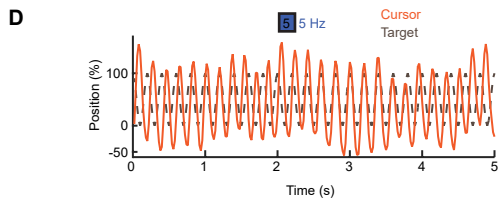
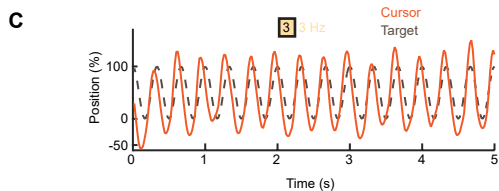
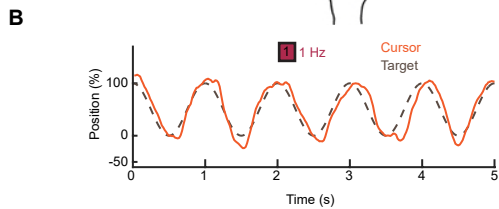
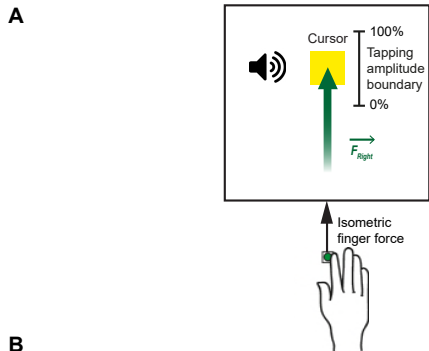
**A**

0 ms delay

**B**

200 ms delay





# Monkey U

